Analog models of oblique rifting in a cold lithosphere

Julia Autin, Nicolas Bellahsen, Laurent Husson, Marie-odile Beslier, Sylvie Leroy, Elia d'Acremont

Analogue models of oblique rifting in a cold lithosphere

[1,2,3]Julia Autin, [1,2]Nicolas Bellahsen, [4]Laurent Husson, [5]Marie-Odile Beslier, [1,2]Sylvie Leroy, [1,2]Elia d'Acremont

Abstract

New lithospheric analogue models of oblique rifting presented here capture the main characteristics of natural oblique rifts and provide insights into the fault evolution, basin segmentation and mantle exhumation occurring during rift localization. We present two models: one with a pre-existing oblique lithospheric weakness (model B) and another with no weakness zone (model A). Both oblique rifts have an obliquity of about 40°. The main results are: (i) The fault populations, especially during the early stages of deformation, are composed of faults that in strike, are largely intermediate between rift-parallel and perpendicular to displacement. This fault population is characteristic of oblique rifts observed in previous studies. (ii) In later stages, faults parallel to the rift become numerous in both models. Buoyancy forces related to thickness variations in the lithosphere during rift localization play a significant role and control the initiation of rift-parallel faults. (iii) During the final stages of extension, in model B the crust is deformed by rift-parallel faults, while in the basins the small-scale deformation pattern is composed of displacement-normal faults. However in model A, displacement-normal faults tend to accommodate most of the extension, controlling its final stages. They probably also control the formation of the ocean-

continent transition, any possible mantle exhumation, as well as the geometry of oceanic accretion centers. These results provide an insight into the possible evolution of the Gulf of Aden conjugate margins, which developed in an oblique context - most probably without any pre-existing rift-parallel localizing heterogeneity in the lithosphere.

1. Introduction

In stable regions with a standard geotherm, the rheology of the lithosphere is usually seen as a brittle/ductile sandwich [brittle and ductile crust, brittle and ductile lithospheric mantle, *Kirby*, 1983]. This rheology, especially the presence of a brittle lithospheric mantle, is one of the main causes of rift localization [*Allemand and Brun*, 1991; *Buck*, 1991; *Hopper and Buck*, 1993; *Brun and Beslier*, 1996; *Frederiksen and Braun*, 2001; *Brun*, 2002]. Inherited lithospheric weakness zones, either in the crust or in the mantle, are another cause of rift localization. As the brittle lithospheric mantle is seen as the most resistant layer, weakness in such a layer is probably the most efficient cause of localized deformation. In this sense, oblique rifting, i.e., a rift that strikes at an angle to the direction of plate motion, is usually seen as a consequence of the presence of a pre-existing oblique lithospheric weakness zone. It may therefore result from a multiphase tectonic history, for example after two successive rifting events such as those observed in the Viking Graben [*Brun and Tron*, 1993; *Faerseth et al.*, 1997].

Obviously, oblique rifting must be studied in 3D. However, currently available methods do not fully satisfy processes of fault geometry and structural evolution numerically and as a result analogue models tend to be used. Investigating rifting processes through analogue modeling on a crustal scale may imply that the system is simplified to that of an extending crust influenced by a basal zone of deformation (extension in the sub-Moho mantle) that acts as the major boundary condition. Indeed, such analogue models (of an extending crust above an oblique velocity discontinuity) have provided important information regarding the evolution of fault patterns in an oblique rift context [*Withjack and Jamison*, 1986; *Tron and Brun*, 1991; *McClay and White*, 1995; *Clifton et al.*, 2000; *Mart and*

50 *Dauteuil*, 2000; *Corti et al.*, 2001; *Corti et al.*, 2003; *Corti*, 2004; *Sokoutis et al.*, 2007]. However, all
51 these models are bounded at depth by the bottom of the box, with the oblique pattern resulting
52 mainly from gravity tectonics without isostatic balancing and involve overestimation of the role of
53 the basal discontinuity. One of the most significant results derived from the modeling of moderate
54 obliquity (from 30° to 60°) is the occurrence of a single main fault population that strikes at an
55 intermediate angle between the trend of the rift and the direction of plate motion. *Withjack and*
56 *Jamison* [1986] showed analytically that in the case of oblique rifting seen as transtension, opening
57 direction and direction of extension are not collinear. In some of the works cited above, rift-parallel
58 faults developed [*Tron and Brun*, 1991; *Mart and Dauteuil*, 2000; *Corti et al.*, 2001; *Corti et al.*, 2003;
59 *Corti*, 2004] while in others they did not [*Withjack and Jamison*, 1986; *McClay and White*, 1995;
60 *Clifton et al.*, 2000], most probably as result of different basal conditions (presence and extent of a
61 ductile layer). In all of them however, only rarely do faults develop normal to plate motion.

62 Applying these models to processes seen in nature yields different results. For oceanic ridges, the
63 models appear to correlate with field observations, with fault populations observed in nature well-
64 predicted by the models [*Clifton et al.*, 2000; *Mart and Dauteuil*, 2000; *Dauteuil et al.*, 2001; *Clifton*
65 *and Kattenhorn*, 2006]. The homogeneity of the newly-created crust in localized and narrow
66 extension zones probably explains this close resemblance. However in continental rifts, the evolution
67 of fault arrays seems more complex. Two rifting events have been documented for the Viking
68 Graben, the first creating a lithospheric weakness zone exploited by the second. For the second
69 event, while *Faerseth et al.* [1997] proposed dextral oblique rifting kinematics, *Brun and Tron* [1993]
70 proposed left-lateral oblique rifting, based on their analogue model results. This example highlights
71 the potential problems which may occur when comparing published analogue models to natural
72 continental rifts.

73 The Gulf of Aden is one of the youngest oceanic basins with oblique kinematics and contains
74 several features characteristic of oblique rifts: (1) The fault strike and kinematics reveal several fault

populations. (2) Fault slip analysis has revealed several directions of extension [see *Bellahsen et al.*, 2006; *d'Acremont et al.*, 2006 and references therein]. Several discrepancies are apparent when comparing the Gulf of Aden with published analogue models. Firstly, three fault populations have been recognized, not two as in the published models. The third class of faults strike perpendicular to the direction of plate motion. Secondly, no lithospheric weakness with the correct orientation has been recognized at the scale of the Gulf and thus rifting in the Gulf of Aden may not be due to any pre-existing lithospheric weakness. Its structure seems to be much more complex than that proposed or simulated in published analogue models.

In order to take into account these particularities and unexplained characteristics, we believe that any model of the Gulf of Aden system must be extended to the whole lithosphere and underlying asthenosphere. Analogue models of oblique rifting in a 3-layered hot extending lithosphere [*Sokoutis et al.*, 2007] have effectively shown that motion-normal faults grow in such oblique rifts. However, in those experiments the rift is wide and the effect of lithospheric oblique weakness does not really cause any oblique rift localization. Models of volcanic passive margins [*Callot et al.*, 2002] have shown that faults highly oblique to displacement can initiate between local weakness zones and thus without any linear weakness zone controlling rift localization. Recent analogue centrifuge experiments have reproduced an oblique rift in a three-layer lithosphere (with a resistant ductile lithospheric mantle) [*Agostini et al.*, 2009]. In these experiments the rift effectively localizes obliquely, while three fault populations are observed and two main phases during rifting are recognized. However, these models do not show the progression from oblique rift initiation to plate rupture. Such late rift evolution would allow comparison with extremely thinned distal passive margins.

We present here new analogue models of oblique rifting (40° obliquity), with rheology consisting of a four-layer lithosphere resting on a low viscosity asthenosphere. The obliquity of the rift is secured by lateral offset of velocity discontinuities and, for the first time, without a weakness zone in the

lithosphere. We show that an oblique rift can develop in a lithosphere wherein the thickness of each layer is initially uniform, i.e. a lithosphere without any pre-existing weakness zone. We finally compare our results to previous analogue models and discuss the structure of the passive margins of the Gulf of Aden in the light of these new results.

2. Model setting and data processing

2.1. Model setup and materials

The models are constructed in a deforming box (56 × 30 × 30 to 50 cm^3; Figure 1) consisting of a bottomless drawer sliding in a rectangular box. The drawer is pulled by a screw jack, which represents the direction of extension. The different lengths of the drawer arms create two lateral velocity discontinuities imposing an oblique zone of deformation (Figure 1).

It is now consensual that an extending continental lithosphere with a normal crustal thickness (about 35 km) and a stable geotherm behaves as a brittle-ductile multilayer [*Kirby*, 1983], and can be simplified at first order by a four-layer type strength profile [e.g., *Davy and Cobbold*, 1988; *Davy and Cobbold*, 1991]. In the laboratory, such a multilayer is modeled using granular materials and silicone. Here, we used a microsphere mix (see below) as an analogue of brittle layers and silicone putties as an analogue of ductile layers.

Our models represent the non-volcanic oblique extension of a resistant lithosphere, as observed in cratons and as such they consisted of an upper brittle crust, a ductile lower crust, an upper brittle lithospheric mantle and a lower ductile lithospheric mantle (see Figure 2 and Table 1 for details). The modeled lithosphere overlies a low viscosity, higher density glucose syrup that mimics the asthenosphere.

2.2. Scaling

The microsphere mix was composed of 4/5 glass to 1/5 hollow aluminum microspheres. The glass microspheres have a density of 1.49 and a frictional angle of 31.5° [D. Rossi, pers. com.], while the

hollow aluminum microspheres have a density of 0.39 and a frictional angle of 24.7° [*Rossi and Storti*, 2003]. This mix provided a granular material with a density of 1.2, comparable to other analogue materials [*Davy and Cobbold*, 1991; *Benes and Davy*, 1996], while its frictional angle of ~30° is comparable to that of Earth materials. The approximate cohesion of such material is low (between few Pa and about 150 Pa). This material was used to model the upper crust (1.5 cm-thick layer) and the lithospheric mantle (0.8 cm-thick layer, see Table 1 and Figure 2).

The silicone putty (SGM36, manufactured by Rhône-Poulenc) was enriched with iron (III) oxide or lead (II) carbonate in order to reach suitable scaled densities and viscosities. The Fe-oxide-enriched 'red silicone' has a density of 1.33 and a Newtonian viscosity of 7.10^4 Pa.s, and is scaled to the properties of the ductile upper mantle (2 cm thick). The Pb-carbonate-enriched 'white silicone' has a density of 1.25 and a Newtonian viscosity of 4.10^4 Pa.s, and corresponds to the ductile lower crust (0.7 cm thick, see Table 1 and Figure 2).

Glucose syrup of high density and very low viscosity was used as an analogue of the asthenosphere. The density increases from top to bottom, in order to model a passive rifting mode.

Thicknesses, viscosities, densities and strain rates were appropriately scaled to simulate an extending continental lithosphere. Scaling of the models to the natural prototype was achieved by maintaining similarity in geometry, dynamics, kinematics and rheology [*Hubbert*, 1937; *Ramberg*, 1981]. The brittle materials were scaled using equation (1):

$$\sigma^* = \rho^*.g^*.L^* , \quad (1)$$

where σ^*, ρ^*, g^* and L^* are the dimensionless stress, density, gravity and model length ratios (model over nature). The models were constructed to a geometrical scale of $L^* = L_{model}/L_{nature} = 0.75 \times 10^{-6}$ (where L_{model} and L_{nature} are the equivalent lengths in model and nature, respectively), i.e. 1.5 cm in the experimental model corresponded to 20 km in nature. The dimensionless gravity ratio was $g^* = 1$ since both models and nature experience the same gravity field. The density ratio was

148 around 0.4 (0.41 in the brittle crust and 0.36 in the brittle mantle). Inputting these values into (1), the
149 stress ratio was therefore set to $\sigma^* = \rho^*.g^*.L^* = 3 \times 10^{-7}$ and thus a scaled analogue material
150 representing the upper crust (cohesion around 30 to 100 MPa) should have a cohesion of around 10
151 to 30 Pa, which is about the same order of magnitude as our granular material.

152 The time scaling for the ductile material is written

153 $$\eta^* = \rho^*.g^*.L^*.\tau^* \quad , \qquad (2)$$

154 where η^* is the viscosity ratio and τ^* is the time ratio. As the viscosity ratio is 4×10^{-17} (natural
155 lower crust: 10^{21} Pa.s and model lower crust: 4.10^4 Pa.s), the time ratio was therefore around $1.33 \times$
156 10^{-10} at the lower crust scale (1 hour in the model corresponds to 0.85 Ma in nature).

157 The experiments were performed with an extension velocity of V = 5 cm/h. In the fast range of
158 rifting processes, this velocity, which corresponds to about 6 cm/yr in nature, is comparable to
159 velocities applied in previous studies - as is the rheology of the model used here [*McClay and White*,
160 1995; *Benes and Davy*, 1996; *Brun and Beslier*, 1996; *Sokoutis et al.*, 2007].

161 ### *2.3. Experiments*

162 From a set of 13 experiments, we focus here on two configurations of oblique extension: a) an
163 experiment with a stratified lithosphere of initially uniformly thick layers (hereafter referred to as
164 model A), where obliquity is induced only by lateral velocity discontinuities; b) an experiment where
165 a weakness zone trends parallel to the direction of obliquity imposed by the lateral velocity
166 discontinuities, and joins them (model B). The weakness zone consists of a locally thinner lithospheric
167 brittle mantle designed prior to the experiment (a thickness of 0.6 cm instead of 0.8 cm along a 5
168 mm-wide zone). The obliquity, i.e., the angle between the direction of extension and the orthogonal
169 to the rift trend, is 40° and is the same in both models. The total displacement is 10 cm in all
170 experiments, corresponding to an extension of 20% throughout the entire model and about 150 to
171 200% throughout the length of the rift for both models. In order to fully observe the fault patterns,

no extra sedimentation was applied during the experiments - since this tends to be an obstacle to clear identification of fault activity. This was achieved by comparing top-view photographs at successive steps of the experiment.

Thermal effects or rheological changes occurring during rifting are not modeled in these experiments and their absence remains a significant limitation of such analogue models. However, they do provide templates for the interpretation of fault patterns and chronology, as well as for lithosphere deformation and possible segmentation in natural rift systems.

2.4. Data processing

Line drawing of faults

Surface photographs and laser scans of the relief were acquired at 2-minute intervals during model evolution. Oblique lightening allows visualization of fault dip on photographs; with north defined as the opening direction, dark faults dip southward and white faults dip northward in Figures 3 and 4. Defined as that part of a fault with uniform orientation, a fault segment provides the direction of extension at its time of initiation. Fault segments were identified on the top views at each step until the fault systems became very complex (~ 30 minutes, 5% extension, Figures 3 and 4). Afterwards, the models were investigated using only the processing output of the DEM (Digital Elevation Model, see below). Segment lengths and azimuths are determined at each step of extension. The number of segments of each fault segment population were calculated through time (Figures 5a and 5d), as was the total fault length for each population (Figures 5b and 5e), and their total length (Figure 5c and 5f). Three main fault populations were observed: (1) N050°-060°E oriented faults, or rift-parallel faults, (2) N060-080°E oriented faults, or intermediate faults, (3) N080-100°E oriented faults, or displacement-normal faults. Zooms of the rift center are also displayed in order to better observe the relationship between fault populations in the highly thinned crust (Figures 6 and 7).

Laser scan processing

The DEMs have a resolution of 0.25 mm in the x, y and z directions. After surface interpolation, each DEM was subtracted from the previous time slice (Figures 8 and 9) in order to obtain differential vertical movements, and hence to infer fault activity during a specific time interval. The surface topography is displayed in map or cross-section view in Figure 10.

Topography corrections for cross-sections

Supplementary photographs and laser scans were recorded during the dismantling of models, providing a DEM of each interface after gradual stripping of the overlying layers (surface, top ductile crust, top brittle mantle and top ductile mantle). The removal of each layer of variable thickness theoretically brings each surface to a new isostatic equilibrium. Taking advantage of this changing isostatic equilibrium, the geometry of each layer was restored prior to stripping off the model. However, because isostatic readjustment was in fact only partially reached, the restored thicknesses were used only as a guide, together with the photographs and DEMs, to reconstruct final lithospheric extension-parallel cross-sections for each model (Figure 11).

3. Results

3.1. Model A

Stage 1

Faults in model A initiate after ~1% extension (Figures 5a), with two zones of deformation near the two lateral velocity discontinuities induced by the asymmetrical drawer arms (Figure 3a). The two en-echelon basins do not overlap, defining a relay zone in the center of the model. This structuration initiates the large-scale en-echelon disposition of the grabens and horsts. The width of the deformed areas reaches 4 cm, accommodated on three main grabens with an intermediate trend (Figure 3a). The subsiding area shows the same intermediate trend (Figure 8a). The deformed zones initiate with displacement-normal (red) and intermediate (green) faults (Figure 3a), propagating towards the

center of the model away from the discontinuities. The two early basins accommodate the deformation during the very first stages of extension.

At between 2 to 3% extension, the relay zone breaks through and rift-parallel faults initiate in the rift center and in connection with the previous intermediate structures (Figure 6a). This occurs together with a sudden increase in the number of fault segments (Figure 5a). Intermediate faults dominate initially, followed by an increasing number of displacement-normal faults and eventually rift-parallel faults (Figure 5a). Rift-parallel faults mainly develop in the center of the model and are short in length (Figure 6b). The relative length of intermediate segments tends to decrease while that of the two other types increases (Figure 5b). Even though intermediate faults have a higher number of segments and greater total length, the total length of rift-parallel and displacement-normal faults increases at a faster rate (Figure 5c). During stage 1, the total length (Figure 5c, black curve) increases quite regularly showing that fault surfaces are continuously created.

Stage 2

The deformation during stages 1 and 2 corresponds to the widening of the two early basins and their propagation towards the center of the model (Figure 6a). At around 3% extension, the number of segments stabilizes at about 350 (Figure 5a), while the total length of the faults increases at a lower rate (Figure 5c). The faults are active, accommodate extension and propagate, but no new segments are created. The relay zone is narrow (4.3 cm, Figure 3b) and is composed of short conjugate rift-parallel faults that join the end of the two offset early basins (Figures 6b). The relay zone widens progressively until it reaches the same width as the lateral deformed zones (8.4 cm, Figure 3d). This widening is mainly controlled by rift-parallel deformation of the two main central horsts and three grabens (Figures 3c and 8c).

After 4-5% extension (Figure 3, stage 2), development of the relay zone is achieved, composed of a combination of the three different fault populations. All major faults are also formed. During this stage, although all fault populations are active, the most significant observation is the relatively high

244 percentage of total fault length composed of rift-parallel fault segments (Figures 5b). These faults,
245 less numerous in the previous stage, are in this stage as abundant as displacement-normal examples.
246 Rift-parallel faults also remain active and numerous during the whole of stage 2 (Figures 3 and 8) and
247 are especially common in the relay zone (Figure 6).

248 *Stage 3*

249 At around 15% extension, the activity of rift-parallel faults tends to lessen, except on the rift
250 shoulders (Figures 8e and 8f). In the rift center, extension is mainly accommodated by displacement-
251 normal faults. These faults are the results of (i) other fault populations that were rotated clockwise
252 during rifting and (ii) new fault segments. Thus spatially continuous horsts, especially rift-parallel
253 ones, which formed during stage 2, are now re-faulted during stage 3 by displacement-normal faults
254 (Figures 6e and 6f).

255 At this stage, the crust (at least the brittle part) is extremely thinned, as attested by the numerous
256 closely-spaced small fault segments, which strike perpendicular to the displacement and are located
257 in the basins.

258 A significant characteristic of the model is the progressive rotation of the crustal blocks (Figures 3f)
259 which are formed along the rift borders with a rift-parallel to intermediate orientation. They then
260 undergo progressive clockwise rotation, which separates the blocks from the rift border, forming a
261 triangular graben. The maximum observed rotation exceeds 20°. These rotations lead to highly
262 deformed areas in the center of the rift zone (Figures 3f). Where opposite rotation zones meet, left-
263 lateral shear zones are induced that accommodate the relative motion between blocks. The left-
264 lateral movements along shear zones are particularly well-defined in the brittle mantle (Figure 12-A).

265 The resulting deformation pattern is very complex. Several phases of deformation are
266 superimposed, particularly in the rift center and in deep grabens. The grabens display various
267 orientations and central structures are rotated or re-faulted.

3.2. Model B

Stage 1

Faults in model B, in which the lithospheric mantle has a non-uniform initial thickness, start to develop after about 1.5% extension (Figures 5), with one main graben located at each lateral velocity discontinuity (Figure 4a). The faults are mainly displacement-normal. With ongoing extension, further faults initiate mainly parallel to the rift and with an intermediate orientation, progressively becoming the two main fault populations (Figures 5e). The rift is narrow and the rift-parallel structure is clearly observed, with a clear oblique rift structure appearing earlier than in model A. This stage (1.5 to 2.8% extension) is characterized by a fairly constant rate of fault segment initiation (Figure 5d, stage 1) and increase in total segment length (Figure 5f).

Stage 2

After around 3% extension, both fault segment initiation and the increase in total segment length slow down (Figures 5d and 5f). Thus although fault segments are active, they propagate only slightly with few segments initiated. Extension is accommodated by the existing segments.

The changes in deformation during stages 1 and 2 lead to the development of a rather narrow well-defined oblique rift zone (4.8 cm, Figure 4b). This zone initiates as two parallel series of en-echelon short grabens separated by an en-echelon horst. These short structures are locally sigmoid and appear to be delineated by intermediate and a few rift-parallel faults. The rifted zone is globally parallel to the underlying heterogeneity in the uppermost brittle mantle.

Long rift-parallel faults then form by coalescence of shorter fault segments. These faults delimit two main rift-parallel grabens separated by one major horst (Figures 4c and 9c). The en-echelon basins are still active on the graben borders (Figures 9c and 9d).

Stage 3

After 10% extension, the central horst begins to be re-faulted by numerous intermediate and rift-parallel faults (Figure 4e). In the grabens, small and closely spaced displacement-normal faults initiate (Figure 7e).

Rotations are not as frequent in model B as they are in model A, since the central horst limits the length of structures and their rotation. However, despite initiating in a rift-parallel direction (Figure 4b), the central horst itself is in a near-intermediate orientation at the end of the experiment (Figure 4f). Small triangular grabens can also be observed on the rift borders.

3.3. Final stage cross-sections and synthesis

Figure 11 presents cross-sections of models A and B in the final stage of the experiments. Some inaccuracies may exist due to their reconstruction from a combination of DEM and top view photographs (see section 2.4.3). However, such issues are related only to the thickness of the layers, not the localization of the major faults, which is well-constrained by major shifts in the scanned surfaces.

In model B, two main basins develop in the brittle crust, located over non-deformed or poorly deformed boudins of brittle mantle. The central horst is located above the ductile mantle heterogeneity, the latter corresponding to a pair of conjugate normal faults in the brittle mantle which delineate a neck where breakup is achieved (Figure 11).

In model A, the total width of the rift zone is more significant as more basins/necks develop in the brittle layers. The main basins in the upper crust are superposed to boudins in the upper brittle mantle. Several neck zones of the brittle mantle have widened out and the breakup is barely attained in the two central ones.

In general, the two oblique rift models present highly segmented basins with an en-echelon pattern (Figure 13) and regardless of the amount of extension, intermediate faults are the most abundant in

315 both (Figure 5, green curves). In both models, rift-parallel faults initiate and become an important
316 fault set in later stages (Figure 5, blue curves), becoming as numerous as displacement-normal faults
317 in model A (Figure 5b) and more numerous in model B (Figure 5e).

318 However, several noteworthy differences are apparent, resulting in deformation being localized in
319 model B and more widely distributed in model A. (i) The total number of segments in model A is
320 twice that observed in model B. (ii) Horsts are more numerous and rise above the mean elevation
321 level in model A, whereas in model B there are few horsts which generally lie under mean elevation
322 except for those on the rift shoulders (Figure 10). (iii) The grabens of model B are deeper.

323 In model A, displacement-normal faults control the final stage of extension (stage 3, Figure 6f),
324 while in model B, large active rift-parallel faults control deformation (although some displacement-
325 normal examples are active in the center of the basin; Figure 7e). Rotations are systematic in both
326 models, but less important in model B. In model A, rotations lead to left-lateral shear zones in the rift
327 center, whereas they only slightly affect the deformation pattern of the central horst in model B.

328 # 4. Discussion

329 ## *4.1. Early stage of oblique rifting (stage 1)*

330 In both analogue models presented here, during the early stages (less than ~3% extension, Figure
331 14-1) the main fault population is composed of faults with intermediate strike (intermediate
332 between being perpendicular to extension and parallel to the rift axis). The models also display
333 displacement-normal faults in the vicinity of the lateral velocity discontinuities (Figures 3a and 4a),
334 the former likely to be edge effects resulting from the latter.

335 The rift localizes obliquely in model A later than in model B because no weakness zone localizes the
336 deformation. Thus in the former, the obliquity of the rift is due to several closely-spaced en-echelon
337 basins, while in model B it is a result of two major zones of deformation, also en-echelon, but here

more widely spaced. This effect is directly linked to the initial structure of the lithosphere, that, when uniform, delays oblique rift localization.

As shown by *Withjack and Jamison* [1986] from analogue and analytical models, an oblique rift first develops under a transtensional regime that induces a slight rotation of the minimum principal stress σ_3 in the applied zone of obliquity. σ_3 is thus slightly oblique to the direction of extension. The resulting fault pattern consists largely of faults with an intermediate strike.

In earlier analogue models [*Tron and Brun*, 1991; *McClay and White*, 1995; *Clifton et al.*, 2000; *Corti et al.*, 2001; *Corti et al.*, 2003; *Corti*, 2004; *Agostini et al.*, 2009], rift obliquity has been modeled as a basal velocity discontinuity moving obliquely to its strike and underlying the crust. Figure 15 shows fault strikes under similar obliquity in the models outlined in this study, those of *Tron and Brun* [1991], *Clifton et al.* [2000], and for the major inland faults onland the Gulf of Aden [*Bellahsen et al.*, 2006]. In good agreement with the prediction of *Withjack and Jamison* [1986], all models and data present a significant peak of intermediate faults (at angles of between 65° and 75° from the direction of displacement). Moreover, this first fault population is also reproduced in other lithospheric-scale and isostatically compensated models containing a heterogeneity, for low to moderate obliquity [*Agostini et al.*, 2009]. These intermediate faults are en-echelon disposed above the weakness zone boundaries, thus delimiting the oblique rift.

In all these aforementioned studies, a similar fault population (intermediate in strike) was observed. Significantly, such a fault population has also been observed and mapped in the Gulf of Aden, suggesting that they are a characteristic feature of oblique rifts. Thus it appears that the analogue models, performed either at crustal or lithospheric scale, accurately reproduce the early stages of oblique continental rifting. In particular, the analogue models consisting of a crust over a basal velocity discontinuity [*Tron and Brun*, 1991; *McClay and White*, 1995; *Clifton et al.*, 2000; *Corti et al.*, 2001; *Corti et al.*, 2003; *Corti*, 2004] have succeeded in capturing the main structural characteristics of oblique rifting, at least in its early stages, without modeling the whole lithosphere.

4.2. Oblique rift evolution (stage 2)

Stage 2 begins when rift-parallel faults become particularly important (Figure 14-2). As opposed to displacement-normal and intermediate faults, the initiation and especially the propagation of such faults are interpreted to be caused by buoyancy forces induced by lithospheric thickness variations across the rift. Thickness variations, together with density contrasts, can effectively produce local stresses (or buoyancy forces) [*Artyushkov*, 1973; *Fleitout and Froidevaux*, 1982] superimposed to the regional far-field stress field (the imposed extension) [*Sonder*, 1990]. This results in the creation of a new stress field related to the angle between the regional stress system and the local structure, as well as to the relative magnitudes of the regional and local stresses. Such a process has already been proposed for the East African Rift System [*Sonder*, 1990; *Zoback*, 1992]. In a rift system where both crust and mantle are thinned, lateral buoyancy variations depend on the density contrast between layers in general, particularly the mantle. A low density crust will be marked by extension in the shoulders and compression in thinned areas. In our models, the asthenospheric mantle is denser than the lithosphere, which similarly affects the stress field and will tend to delocalize the deformation. Conversely, if the lithospheric mantle was denser than the asthenosphere, a competing mechanism would arise and cause extension in the rift center and compression in the shoulders [active rift, e.g. *Huismans et al.*, 2001], making the rifts even more localized. In addition to local stresses, oblique weakening of the lithosphere (pre-existing or acquired during the model) will naturally induce faults that are parallel to the weakness. Both phenomena contribute to the final rift-parallel structuration of the rifts.

In model B, the rift is obliquely localized above the pre-existing weakness zone in the lithospheric brittle mantle (Figure 4-c). Model thinning along this rifted zone creates buoyancy forces that are responsible for extensional stresses oriented perpendicular to the rift. These local stresses are responsible for rift-parallel faults. The resulting geometry - with a central horst above the weakness zone - is similar to natural rifts observed in the oblique East African rift [e.g. Rwenzori Monts, Amaro horst, Lake Tanganyika, *Ebinger et al.*, 1993; *Kusznir et al.*, 1995; *Upcott et al.*, 1996; *Ring*, 2008] and

389 seems to be due to the phase opposition of deformation in the crust and the mantle [*Brun and*
390 *Beslier*, 1996, see further].

391 In model A, a relay zone forms between the two shifted discontinuities, as deformation propagates
392 toward the center of the model (Figure 3-b). The first rift-parallel faults initiate when this relay
393 breaks through, most probably in an un-thinned lithosphere. Rift-parallel faults therefore initiate
394 obliquely in order to link the two lateral deformed zones, in response to rotated extensional stresses.
395 Such a mechanism was also suggested by *Huchon and Khanbari* [2003] to explain the rift-parallel
396 faults and rift-perpendicular extension direction observed along the Gulf of Aden. The authors also
397 noticed that this could not be a valid explanation for the whole rift, but only locally. Our results tend
398 to confirm the hypothesis that relay faults form in some places between en-echelon basins.

399 Once such faults are active and start thinning the crust, the rift tends to localize at a large scale
400 along an oblique trend, with local stresses due to crustal thickness variation then also acting to
401 enhance such rift-parallel faults. In such zones, the buoyancy stresses will be perpendicular to the
402 deformed zone controlled by the earlier relay faults.

403 In model A, the rift has a more complex geometry, the basins in the crust have a variety of
404 orientations and thus rift-parallel faults are less numerous (although they are present, also in the
405 zones where the initial basins are displacement-normal). This observation highlights the importance
406 of buoyancy forces. In model B their importance is enhanced, since the experimental setup initially
407 makes the model intrinsically prone to rift-parallel faulting. Conversely in model A, all lithospheric
408 layers are uniformly thick and buoyancy forces are null in the first stages. It is only after the rift has
409 created them that they may contribute to the stress balance. Indeed, one of the goals of these
410 experiments was to test whether oblique buoyancy stresses could emerge out of a uniformly thick
411 lithosphere and fault the lithosphere obliquely to plate motion.

4.3. Rift localization (stage 3)

In both models, once the rift localizes, the rate at which new fault segments initiate tends to decrease, with the deformation mostly accommodated by previously-initiated fault segments. However once the rift is mature (stage 3), the formation of new segments resumes (Figure 14-3).

In model B, new intermediate and rift-parallel faults crosscut the central horst (Figure 7e). This is especially clear in the central horst and on the borders of the rift. Displacement-normal faults then localize in the main deep grabens, as seen in the final line drawing (Figure 13, right). In model A, displacement-normal faults crosscut intermediate and rift-parallel structures, except on the rift borders where rift-parallel faults are still active (Figures 6e and 6f). This is consistent with other analogue models in which the faults close to the rift-parallel direction are border faults [here referring to the faults at the margin of the deformed zone, *Tron and Brun*, 1991, see Figure 3; *McClay and White*, 1995; *Agostini et al.*, 2009].

During the late stage (stage 3) in both models, displacement-normal faults initiate only in the center of the rifted zone, where the brittle crust is significantly thinned (down to few mm, attested by the fault spacing). Just below this area, although the ductile crust may not be as thin as the overlying brittle part (Figure 11), it is most probably thinned laterally where it connects deformed brittle crust and brittle mantle zones. Where the brittle crust is thinned, crustal thickness variations probably tend to be small, most likely making buoyancy stresses very low. The stress state is then controlled by the far field boundary conditions and new faults initiate perpendicular to the direction of displacement.

Similar faults have also been described in recent three-layer analogue models of oblique rifting [*Agostini et al.*, 2009]. However, at similar orientation, these faults are slightly oblique and most probably correspond to faults created during the equivalent of our stage 2.

Moreover, in our models, as the thinned parts of the lithosphere localize the deformation, the development of rift-parallel faults on the rift borders decreases. This localization of deformation in

437 the rift center can be observed in the Main Ethiopian rift, where mid-Miocene border faults bound
438 active displacement-normal magmatic segments [*Ebinger and Casey*, 2001].

439 At the scale of the rifted area, a comparison of our models and the orthogonal lithospheric-scale
440 experimental models of *Brun and Beslier* [1996] shows that similar processes control the localization
441 of deformation at depth regardless of the extension obliquity. Final cross-sections of the three types
442 of model are presented in Figure 11. Analogue materials, layer thicknesses and extension velocities
443 are comparable in orthogonal and oblique models. The orthogonal experiment is uniform, i.e., with
444 no pre-existing rheological weaknesses. In this model the deformation pattern is controlled by the
445 boudinage of the two high strength brittle layers. This necking instability is in phase opposition, with
446 surface grabens corresponding at depth to boudins of brittle mantle, and the surface horsts to
447 thinned neck zones. The thickness variations in the ductile crust are a consequence of horizontal
448 shear, which accommodates the differential extension in each brittle layer, and therefore constitutes
449 a decoupling level between the upper crust and the mantle. The breakup of the brittle mantle occurs
450 in a single neck zone, leading to the superposition of two conjugate normal shear zones, one in the
451 ductile lower crust and one in the ductile mantle [*Brun and Beslier*, 1996]. As extension proceeds,
452 localization of the deformation in this lithospheric weakness zone induces necking of the whole
453 lithosphere and extreme thinning of the crust in one of the crustal grabens (Figure 11).

454 Similarly, in both oblique rifted models, the two brittle-ductile systems (crust and mantle) are
455 globally in phase opposition, with thinned brittle crust being above unthinned brittle mantle and vice
456 versa (Figure 11). It is noteworthy that even in model B, boudinage controlled the initial deformation
457 of the layer, with the heterogeneity being responsible only for localization of the breakup in one of
458 the neck zones. The two crustal grabens closest to the mantle breakup are preferentially enlarged. In
459 model A, for a comparable amount of extension the rift zone is wider because of the en-echelon
460 pattern of deformation. This pattern in the brittle mantle (Figure 12A) prevents efficient localization

of the deformation at depth and delays the preferential enlargement of one of the grabens in the crust.

4.4. Onset of possible mantle exhumation

According to the orthogonal lithospheric-scale experimental models of *Brun and Beslier* [1996], the first stage in mantle exhumation is the breakup of the brittle mantle which localizes the deformation at depth. The consequent necking of the whole lithosphere leads to uplift of the mantle along major normal shear zones and to extreme thinning of the crust in one of the grabens. This can result in the complete exhumation of the mantle in the crustal breakup zone (Figure 11) [*Brun and Beslier*, 1996].

The main difference between oblique and orthogonal models is the width of the rifted zone. In orthogonal experiments, complete crustal breakup and consequent mantle exhumation occurs at less than 10% extension (Figure 11) [*Brun and Beslier*, 1996]. In contrast, even though oblique models simulate an extension twice as great (~20%), the ductile mantle does not reach the surface, even when breakup of the brittle mantle is achieved. This could be partly explained by sedimentation occurring in the orthogonal models, since none is reproduced in the oblique models. Indeed, *Bialas and Buck* [2009] have shown that syn-rift sedimentation increases rift localization. In model B, the ductile mantle heterogeneity below the central horst corresponds to a neck in the brittle mantle where breakup is achieved (Figure 11). Remarkably, the top view of the brittle mantle shows that this breakup occurs along the whole rifted area (Figure 12). With this geometry being close to that of the orthogonal model, ongoing extension, together with syn-rift sedimentation, would probably lead to mantle exhumation. In oblique model A, the en-echelon pattern of the rifted zone, especially in the brittle mantle (Figure 12-A), prevents localization of thinning along a continuous zone and as a result deformation is more diffuse in the brittle crust. The rifted area is consequently wider and mantle exhumation is barely achieved.

These models could be useful for studying the occurrence of mantle exhumation in an oblique context on natural margins, such as the south Australian margin (obliquity ~45°) [*Willcox and Stagg*,

1990]. Further implications for deep layer exhumation under oblique extension are beyond the scope of this paper and require further investigation of oblique model cross-sections.

4.5. Block rotation

Block rotation is observed in both models, although on a much larger scale in model A than in model B. Rotations are clockwise in both models, consistent with the kinematics of oblique rifting (right lateral). Some horsts rotate by about 20°. Rotation also induces opening of triangular grabens (e.g., Figure 3f). They are narrow near the rift border but along strike toward the rift center they become much wider, as more extension is accommodated in such a location. In the rift center, block rotation induces the formation of left-lateral steep shear zones, especially apparent on the top view of the brittle mantle (Figure 12-A). These shear zones may represent proto-transfer zones (and proto-transform faults) and their spacing is linked to the scale of the rotated blocks which is in turn most probably influenced by both rift obliquity and crustal thickness. These proto-transfer zones are much less discrete than natural transfer zones or transform faults. In the models, as well as in early rift systems, the deformation is relatively well-distributed - much more so than in oceanic areas for instance. As shown further down, in the Gulf of Aden, transform faults almost never correspond to transfer faults in the proximal margin. Through time, as the rift localizes in its center, the transfer zones will also localize along transfer faults. Moreover, during ocean-continent transition and oceanic accretion (deformation being even more localized), real and discrete transfer/transform faults will actively separate segments.

Rotations are less common in model B, while no transverse steep shear zones are observed either at surface level or at depth. Thus model A favors block rotation, since all faults have mainly dip slip displacement transtensionnal kinematics, inducing rotation. In contrast, model B favors rift-parallel faults, which obviously prevent block rotation. These rift-parallel faults are more numerous than in model A and may correspond to the larger amount of rift perpendicular extension observed. Under

such kinematics they would be dip-slip, with no rotation necessary. However, some oblique slip on the rift-parallel faults that would also prevent block rotation cannot be ruled out.

As a consequence, block rotations dissect the horst and graben structures in the rift center. The extensional features are then shorter and more discontinuous near the rift center than on the rift borders. These observations have noteworthy implications for the comprehension of the structure of the conjugate margins of oblique rifts. Analogue modeling suggests that the faults presently observed in distal parts of such passive margins, near the ocean-continent transition, do not show their initial orientation, whereas the more proximal parts of the margins, especially the emerged parts, may better preserve initial fault trends until the end of rifting. Moreover, while block rotation occurs, new faults initiate in these rotating blocks. Their final shape is rotated and re-faulted obliquely.

Such block rotations have been observed in paleomagnetism measurements of the young oblique Main Ethiopian rift [*Kidane et al.*, 2009]. These results indicate ~7° counterclockwise block rotation, consistent with the transtensional deformation recorded occurring on the magmatic segment. We thus believe that block rotation may be an important feature in oblique rift evolution, especially in the rift center, and that it may also explain some of the structural complexities observed in the Gulf of Aden.

4.6. Application: the oriental Gulf of Aden

A variety of physical models have been used to interpret the geometry and evolution of fracture populations that form on mid-oceanic ridges and continental rifts during oblique extension [*Withjack and Jamison*, 1986; *Tron and Brun*, 1991; *McClay and White*, 1995; *Clifton et al.*, 2000; *Mart and Dauteuil*, 2000; *Corti et al.*, 2001; *Dauteuil et al.*, 2001; *Corti et al.*, 2003; *Corti*, 2004; *Sokoutis et al.*, 2007]. The structure and evolution of the Gulf of Aden has already been studied in the clay analogue and analytical models of *Withjack and Jamison* [1986]. They noted that the intermediate fault

535 population of the Gulf was an important one, in good agreement with their models and corroborated
536 by ours. However, both onshore and offshore data were rather scarce at the time of their study. New
537 data are now available which provide excellent coverage of these young conjugate passive margins,
538 well-preserved beneath a thin post-rift sedimentary cover, and allow the study of young oblique rift
539 structuration and breakup processes. Onshore and offshore data from Oman [*Fournier et al.*, 2004;
540 *d'Acremont et al.*, 2005; *Bellahsen et al.*, 2006] and Yemen [*Huchon and Khanbari*, 2003] confirm the
541 above conclusions, but also show some complexities that can be more fully understood in the light of
542 our models.

543 The Gulf of Aden strikes N070°, forming under the influence of a supposedly N020°-trending far
544 field extension of the Afar hot spot to the west, and maybe of the propagating Carlsberg ridge to the
545 east. The obliquity is around 40°. Around 30-40 Ma ago, the (still-active) subduction of the Tethyan
546 Ocean under the Zagros and Makran, with its starting collision in the Bitlis, could have led to
547 extensional stresses being put on the African plate [*Bellahsen et al.*, 2003]. The Gulf opened along an
548 orientation that was not inherited and thus seems to be newly created, as discussed in *Bellahsen et*
549 *al.* [2003].

550 Three fault populations (extension-normal, rift-parallel and intermediate, see Figure 16) are
551 observed on the onshore margins, as well as several directions of extension, in Oman [*Lepvrier et al.*,
552 2002; *Fournier et al.*, 2004; *Bellahsen et al.*, 2006], Yemen [*Huchon et al.*, 1991; *Huchon and*
553 *Khanbari*, 2003] and on Socotra Island [*Fournier et al.*, 2007]. According to the faulting chronologies,
554 both counter-clockwise [N020°E extension toward N160°E extension, *Lepvrier et al.*, 2002; *Huchon*
555 *and Khanbari*, 2003; *Bellahsen et al.*, 2006; *Autin*, 2008] and clockwise rotation [*Fournier et al.*, 2004;
556 N160°E extension toward N020°E extension, *Autin*, 2008] occurred during rifting.

557 The Gulf of Aden is highly segmented, with first-order and second-order segmentations [*Leroy et*
558 *al.*, 2004; *d'Acremont et al.*, 2005]. Offshore, near the ocean-continent transition, both faults and
559 basins mainly strike perpendicular to the Gulf opening [*d'Acremont et al.*, 2005]. On the distal poor-

560 magmatic northeastern margin (offshore Oman, Figure 16), grabens present triangular morphology:
561 they open and deepen toward the east [*Autin*, 2008]. The ocean-continent transition (OCT) most
562 likely exhibits exhumed serpentinized mantle on the northern margin [*d'Acremont et al.*, 2006; *Leroy*
563 *et al.*, 2010].

564 The models presented in this study were elaborated to be consistent with the obliquity of the Gulf
565 of Aden. The four-layer rheology corresponds to a cold lithosphere, deformed during the Tertiary
566 non-volcanic rifting of the Gulf of Aden. However, this rheology is only representative of the oriental
567 Gulf of Aden, since the western part is likely influenced by the Afar hot spot. The results presented by
568 our analogue models lead us to propose the following ideas for the Gulf of Aden:

569 (i) The models could explain the two rotations of the direction of extension in the Gulf of Aden and
570 allow the proposal of a relative chronology: (1) Both models suggest that the observed counter-
571 clockwise rotation results from buoyancy stresses caused by crustal and lithospheric thickness
572 variations on the rift border, as already proposed by *Bellahsen et al.* [2006]. In such a rift-normal
573 stress regime (N160°E extension), rift-parallel faults may be activated and displacement-normal ones
574 reactivated obliquely, as observed in some places in the field [*Huchon and Khanbari*, 2003; *Bellahsen*
575 *et al.*, 2006]. We suggest that the stress rotation in the Gulf of Aden was due to buoyancy forces in
576 the lithosphere (because of the density contrast, even if the mantle is denser; see section 4.2). (2)
577 The observed clockwise rotation may be related to a late rotation of stresses in the rift center.
578 Indeed, in both models the crust at the rift center is highly thinned and thickness variations become
579 smaller, making buoyancy stresses accordingly low. Thus the stress regime is again dominated by far
580 field boundary conditions, i.e., N-S to N020°E as suggested by *d'Acremont et al.* [2006], that control
581 the structure of OCT and early accretion segments.

582 (ii) The highly segmented nature of the Gulf of Aden (Figure 16) may be due to rift obliquity
583 inducing block rotation. This would explain the structural features of the natural oblique rifts: (1) In
584 such rifts, segmentation is structured by numerous transfer and transform zones. In model A, block

585 rotations cause steep shear in the rift center. The steep faults are roughly parallel to the opening
586 direction and well-oriented to becoming transfer and potentially transform faults, as observed in
587 natural rifts. One can hypothesize that these transfer faults localize the transform zones that initiate
588 during the formation and deformation of the OCT and/or during the final stages of rifting
589 [*d'Acremont et al.*, 2006]. It is noteworthy that transfer faults in the Gulf of Aden are observed only
590 offshore, i.e., in the distal highly-stretched part of the margin. They are almost absent in the proximal
591 part. This is well reproduced by the models, where transfer faults initiate and localize only in the
592 model center. In the rift borders, deformation is 'distributed' and transfer faults cannot localize. (2)
593 Oblique rifts show horsts of short length in the distal margin (Figure 16), which may be a
594 consequence, as shown in both models, of block rotation. Indeed, rotated blocks are faulted in
595 several directions during ongoing deformation, resulting in short horsts (shorter than in orthogonal
596 rifts). Thus it could be suggested that the highly non-cylindrical structures revealed by seismic
597 reflection imaging (Figure 16) are due to block rotation and horst re-faulting. (3) In the eastern
598 margins of the Gulf of Aden, grabens with triangular morphology are observed [*Autin et al.*, 2010;
599 *Leroy et al.*, 2010] (Figure 16). These drastic along-strike variations in margin shape could result from
600 the block rotation that occurs mainly in model A. Such a triangular morphology is especially apparent
601 in the OCT offshore of Oman. This suggests that if any OCT formation or mantle exhumation occurs,
602 then it will take place in only a short length of the en-echelon structured margin. The final stages of
603 rifting and possible mantle exhumation thus occur in en-echelon zones, controlled by displacement-
604 normal faults as mentioned earlier. This morphology thus controls the initiation of en-echelon
605 oceanic accretion centers. Indeed, oceanic accretion occurs in non-oblique, opening perpendicular
606 segments of a few tens of kilometers each [*d'Acremont et al.*, 2010].

607 (iii) The Gulf of Aden displays an en-echelon disposition of main oceanic basins and fault pattern
608 (Figure 16), suggesting an en-echelon disposition for the thinnest parts of the lithosphere - as
609 observed only in model A (Figures 12 and 14-3). This is accompanied by the displacement-normal
610 direction of the central structures, from late syn-rift to the present. The distal triangular grabens also

611 suggest that important block rotations occur, even in the center of the rift, with again only model A
612 displaying significant block rotation affecting the central part of the rift. Finally, strong segmentation
613 seems to initiate in the Gulf as early as late syn-rift. This is possibly a result of block rotation inducing
614 the formation of displacement-parallel shear zones, as observed in the upper mantle of model A.

615 (iv) There are no currently available arguments that suggest oblique inheritance in the Gulf of Aden.
616 Reactivated Mesozoic basins (N110°), Paleozoic strike-slip (N120°) and extensive N045° systems are
617 not oriented to induce the obliquity of the Gulf of Aden (N070°). The dispositions of the Carlsberg
618 Ridge in the east and the Afar hot spot in the west are therefore probably responsible for controlling
619 the direction of the Gulf [*Bellahsen et al.*, 2003; *Hubert-Ferrari et al.*, 2003]. Given this and the
620 differences between models A and B, we believe that the Gulf of Aden opened obliquely without
621 reactivating large-scale lithospheric weaknesses. Indeed, the fault pattern of the Gulf and model A
622 are extremely similar. Drastic lateral variations (as triangular grabens) are also present and could
623 indicate horst rotations that would favor the development of transfer zones - and thus also of the
624 high segmentation observed in the Gulf. In the Gulf of Aden, the en-echelon structuration of both the
625 spreading centers and the OCT indicate that this geometry was acquired in late syn-rift or even
626 sooner, as suggested only by model A. This study therefore reaffirms the model of *Bellahsen et al.*
627 [2006], in which the obliquity of the Gulf of Aden does not depend on an inherited lithospheric
628 heterogeneity.

629 Finally, it should be noted that the analogue models cannot reproduce thermal effects or
630 rheological changes occurring in the lithosphere. However in such a non-volcanic context, thermal
631 evolution may induce melting in only the latest stages of rifting. The structural changes that it implies
632 will therefore probably only amplify the earlier evolution of rift localization. Moreover, following the
633 study of *Pérez-Gussinyé and Reston* [2001], the ranges of rift duration (1.7 Ma) and beta factors (5) of
634 the models suggest that rheological changes would have occurred along with the entire
635 embrittlement of the lower crust, allowing both water to reach the mantle and peridotite

636 serpentinization. The same conclusions were proposed for the Gulf of Aden with a stretching factor
637 of 4-5 for a maximum rifting duration of 15-18 Ma [*Autin et al.*, 2010].

638 # Conclusion

639 In both models, fault pattern evolution indicates how the rift localizes. In the first stage,
640 intermediate faults (oblique to both the rift axis and the perpendicular to the extension) are most
641 significant, especially in model B due to the overall kinematics of the oblique rift. These were also
642 predicted by previous analogue models.

643 In the second stage the rift localizes along the oblique zone, especially through the initiation of rift-
644 parallel faults, probably due to crustal and lithospheric thickness variations that induce buoyancy
645 stresses. Extension becomes oriented along the thickness gradient, i.e., normal to the rift axis.

646 Once the rift has thinned sufficiently, deformation localizes in the rift center where no significant
647 crustal thickness variation occurs. In model A, no buoyancy stresses perturb the far field stress and
648 faults perpendicular to the far-field extension develop, resulting in zones of extreme thinning that
649 remain en-echelon. These are believed to control the structure of the OCT and the geometry of the
650 accretion centers. In model B, faults perpendicular to the far field extension as well as rift-parallel
651 ones control the late stages of deformation. Thus in this case the zone of extreme thinning is aligned
652 with the rift axis.

653 These characteristics enable an explanation to be made of the structures observed in the Gulf of
654 Aden and their evolution. The structural evolution described by the models offers a clear
655 understanding of the hierarchical relationship between far-field and buoyancy stresses through time
656 and allows the establishment of the timing of faults with a resolution that is beyond the current state
657 of knowledge of the Gulf of Aden. Because our models show that oblique rifts that develop in
658 isotropic lithospheres feature a range of structures that resemble much of the temporal and spatial

659 structure of the Gulf of Aden, we emphasize that the rift grew obliquely in the absence of significant
660 pre-existing lithospheric weakness.

661

662 # Acknowledgements

663 The reviewers, C. Ebinger and R. Huismans, as well as the editor, O. Oncken, significantly improved
664 the manuscript by their constructive remarks. We thank F. Funiciello and C. Faccenna for their
665 advices, comments and help in the Laboratory of experimental geology of the University of Rome III.
666 We thank J.P. Brun for stimulating discussions, and W. Royden and MIT for technical support. We
667 also would like to thank D. Rossi for making available his rheological measurements. Figures 3, 4, 8, 9,
668 10 and 11 were produced with the GMT software package [*Wessel and Smith*, 1995]. This study is a
669 contribution of the GDR "Marges", the "Actions Marges" and ANR YOCMAL.

670

References

Agostini, A., G. Corti, A. Zeoli, and G. Mulugeta (2009), Evolution, pattern and partitioning of deformation during oblique continental rifting: Inferences from lithospheric-scale centrifuge models, *Geochem. Geophys. Geosyst.*, *10*(Q11015), doi:10.1029/2009GC002676.

Allemand, P., and J. P. Brun (1991), Width of continental rifts and rheological layering of the lithosphere, *Tectonophysics*, *188*, 63-69.

Artyushkov, E. V. (1973), Stresses in the lithosphere caused by crustal thickness inhomogeneities, *J. Geophys. Res.*, *78*, 7675-7708.

Autin, J. (2008), Déchirure continentale et segmentation du Golfe d'Aden oriental en contexte de rifting oblique, PhD thesis, Université Paris VI, France.

Autin, J., S. Leroy, M.-O. Beslier, E. d'Acremont, P. Razin, A. Ribodetti, N. Bellahsen, C. Robin, and K. Al Toubi (2010), Continental break-up history of a deep magma-poor margin based on seismic reflection data (northeastern Gulf of Aden margin, offshore Oman), *Geophys. J. Int.*, *180*(2), 501-519, doi: 510.1111/j.1365-1246X.2009.04424.x.

Bellahsen, N., C. Faccenna, F. Funiciello, J.-M. Daniel, and L. Jolivet (2003), Why did Arabia separate from Africa? Insights from 3-D laboratory experiments, *Earth Planet. Sci. Lett.*, *216*, 365-381.

Bellahsen, N., M. Fournier, E. d'Acremont, S. Leroy, and J.-M. Daniel (2006), Fault reactivation and rift localization: the northeastern Gulf of Aden margin, *Tectonics*, *25*, 14 p.

Benes, V., and P. Davy (1996), Modes of continental lithospheric extension: experimental verification of strain localization processes, *Tectonophysics*, *254*, 69-87.

Beydoun, Z. R., and H. R. Bichan (1969), The geology of Socotra Island, Gulf of Aden, *Q. J. Geol. Soc. Lond.*, *125*, 413-446.

Bialas, R. W., and W. R. Buck (2009), How sediment promotes narrow rifting: Application to the Gulf of California, *Tectonics*, *28*(4), TC4014.

Birse, A. C. R., W. F. Bott, J. Morrison, and M. A. Samuel (1997), The Mesozoic and early tertiary tectonic evolution of the Socotra area, eastern Gulf of Aden, Yemen, *Mar. Pet. Geol.* , *14*(6), 675-684.

Brannan, J., K. D. Gerdes, and I. R. Newth (1997), Tectono-stratigraphic development of the Qamar basin, eastern Yemen, *Mar. Pet. Geol.* , *14*(6), 701-730, IN707-IN712.

Brun, J.-P., and M.-O. Beslier (1996), Mantle exhumation at passive margins, *Earth Planet. Sci. Lett.*, *142*, 161-173.

Brun, J. P. (2002), Deformation of the continental lithosphere: Insights from brittle-ductile models, in *Deformation mechanisms, rheology and tectonics : Current status and future perspectives*, edited by S. De Meer, et al., pp. 355-370, Geological Society of London, Special Publication.

705 Brun, J. P., and V. Tron (1993), Development of the North Viking Graben: inferences from laboratory
706 modelling, *Sediment. Geol.*, *86*(1-2), 31-51.

707 Buck, W. R. (1991), Modes of Continental Lithospheric Extension, *J. Geophys. Res.*, *96*(B12), 20161-
708 20178.

709 Callot, J. P., L. Geoffroy, and J. P. Brun (2002), Development of volcanic passive margins: three-
710 dimensional laboratory models, *Tectonics*, *21*(6), 1052.

711 Clifton, A. E., and S. A. Kattenhorn (2006), Structural architecture of a highly oblique divergent plate
712 boundary segment, *Tectonophysics*, *419*(1-4).

713 Clifton, A. E., R. W. Schlische, M. O. Withjack, and R. V. Ackermann (2000), Influence of rift obliquity
714 on fault-population systematics: results of experimental clay models, *J. Struct. Geol.*, *22*, 1491-1509.

715 Corti, G. (2004), Centrifuge modelling of the influence of crustal fabrics on the development of
716 transfer zones: insights into the mechanics of continental rifting architecture, *Tectonophysics*, *384*(1-
717 4), 191-208.

718 Corti, G., M. Bonini, S. Conticelli, F. Innocenti, P. Manetti, and D. Sokoutis (2003), Analogue modelling
719 of continental extension: a review focused on the relations between the patterns of deformation and
720 the presence of magma, *Earth-Sci. Rev.*, *63*(3-4), 169-247.

721 Corti, G., M. Bonini, F. Innocenti, P. Manetti, and G. Mulugeta (2001), Centrifuge models simulating
722 magma emplacement during oblique rifting, *J. Geodyn.*, *31*(5), 557-576.

723 d'Acremont, E., S. Leroy, M.-O. Beslier, N. Bellahsen, M. Fournier, C. Robin, M. Maia, and P. Gente
724 (2005), Structure and evolution of the eastern Gulf of Aden conjugate margins from seismic
725 reflection data, *Geophys. J. Int.*, *160*, 869-890.

726 d'Acremont, E., S. Leroy, M. Maia, P. Gente, and J. Autin (2010), Volcanism, jump and propagation on
727 the Sheba ridge, eastern Gulf of Aden: segmentation evolution and implications for oceanic accretion
728 processes, *Geophys. J. Int.*, *180*(2), 535-551, doi: 510.1111/j.1365-1246X.2009.04448.x.

729 d'Acremont, E., S. Leroy, M. Maia, P. Patriat, O. Beslier Marie, N. Bellahsen, M. Fournier, and P. Gente
730 (2006), Structure and evolution of the eastern Gulf of Aden; insights from magnetic and gravity data
731 (Encens-Sheba MD117 cruise), *Geophys. J. Int.*, *165*(3), 786-803.

732 Dauteuil, O., P. Huchon, F. Quemeneur, and T. Souriot (2001), Propagation of an oblique spreading
733 center: the western Gulf of Aden, *Tectonophysics*, *332*, 423- 442.

734 Davy, P., and P. R. Cobbold (1988), Indentation tectonics in nature and experiment. I: Experiments
735 scaled for gravity, *Bull. Geol. Inst. Uppsala*, *14*, 129-141.

736 Davy, P., and P. R. Cobbold (1991), Experiments on shortening of a 4-layer model of the continental
737 lithosphere, *Tectonophysics*, *188*(1-2), 1-25.

738 Ebinger, C. J., and M. Casey (2001), Continental breakup in magmatic provinces: An Ethiopian
739 example, *Geology*, *29*(6), 527-530.

740 Ebinger, C. J., T. Yemane, G. Woldegabriel, J. L. Aronson, and R. C. Walter (1993), Late Eocene-Recent
741 volcanism and faulting in the southern main Ethiopian rift, *J. Geol. Soc.*, *150*(1), 99-108.

742 Faerseth, R. B., B. E. Knudsen, T. Liljedahl, P. S. Midboe, and B. Soderstrom (1997), Oblique rifting and
743 sequential faulting in the Jurassic development of the northern North Sea, *J. Struct. Geol.*, *19*(10),
744 1285-1302.

745 Fantozzi, P. L. (1996), Transition from continental to oceanic rifting in the Gulf of Aden: structural
746 evidence from field mapping in Somalia and Yemen, *Tectonophysics*, *259*(4), 285-311.

747 Fleitout, L., and C. Froidevaux (1982), Tectonics and topography for a lithosphere containing density
748 heterogeneities, *Tectonics*, *1*(1), 21-56.

749 Fournier, M., N. Bellahsen, O. Fabbri, and Y. Gunnell (2004), Oblique rifting and segmentation of the
750 NE Gulf of Aden passive margin, *Geochem. Geophys. Geosyst.*, *5*(11), 24 p.

751 Fournier, M., P. Huchon, K. Khanbari, and S. Leroy (2007), Segmentation and along-strike asymmetry
752 of the passive margin in Socotra, eastern Gulf of Aden: Are they controlled by detachment faults?,
753 *Geochem. Geophys. Geosyst.*, *8*(3).

754 Frederiksen, S., and J. Braun (2001), Numerical modelling of strain localisation during extension of
755 the continental lithosphere, *Earth Planet. Sci. Lett.*, *188*(1-2), 241-251.

756 Hopper, J. R., and W. R. Buck (1993), The initiation of rifting at constant tectonic force: role of
757 diffusion creep, *J. Geophys. Res.*, *98*, 16213–16221.

758 Hubbert, M. K. (1937), Theory of scale models as applied to the study of geologic structures, *Bull.*
759 *Geol. Soc. Am.*, *48*(10), 1459-1519.

760 Hubert-Ferrari, A., G. King, I. Manighetti, R. Armijo, B. Meyer, and P. Tapponnier (2003), Long-term
761 elasticity in the continental lithosphere; modelling the Aden ridge propagation and the Anatolian
762 extrusion process., *Geophys. J. Int.*, *153*, 111-132.

763 Huchon, P., F. Jestin, J. M. Cantagrel, J. M. Gaulier, S. A. Kirbash, and A. Gafaneh (1991), Extensional
764 deformation in Yemen since Oligocene and the Africa-Arabia-Somalia triple junction, *Ann. Tect.*, *V*,
765 p.141-163.

766 Huchon, P., and K. Khanbari (2003), Rotation of the syn-rift stress field of the northern Gulf of Aden
767 margin, Yemen, *Tectonophysics*, *364*(3-4), 147-166.

768 Huismans, R. S., Y. Y. Podladchikov, and S. Cloething (2001), Transition from passive to active rifting:
769 relative importance of the asthenospheric doming and passive extension of the lithosphere, *J. Geol.*
770 *Res.*, *106*(B6), 11,271-211,291.

771 Khanbari, K. (2000), Propagation d'un rift océanique: Le Golfe d'Aden Ses effets structuraux sur la
772 marge yéménite, PhD thesis, 204 pp, Laboratoire de Géologie, Ecole Normale Supérieure, Paris, Paris.

773 Kidane, T., Y.-I. Otofuji, Y. Komatsu, H. Shibasaki, and J. Rowland (2009), Paleomagnetism of the
774 Fentale-magmatic segment, main Ethiopian Rift: New evidence for counterclockwise block rotation
775 linked to transtensional deformation, *Phys. Earth Planet. Inter.*, *176*(1-2), 109-123.

776 Kirby, S. H. (1983), Rheology of the Lithosphere, *Rev. Geophys.*, *21*(6), 1458-1487.

777 Kusznir, N. J., A. M. Roberts, and C. K. Morley (1995), Forward and reverse modelling of rift basin
778 formation, *Geol. Soc. London, Spec. Publ.*, *80*(1), 33-56.

779 Lepvrier, C., M. Fournier, T. Bérard, and J. Roger (2002), Cenozoic extension in coastal Dhofar
780 (southern Oman): implications on the oblique rifting of the Gulf of Aden, *Tectonophysics*, *357*, 279–
781 293.

782 Leroy, S., et al. (2004), From rifting to spreading in the eastern Gulf of Aden: a geophysical survey of a
783 young oceanic basin from margin to margin, *Terra Nova*, *16*(4), 185-192.

784 Leroy, S., et al. (2010), Contrasted styles of rifting in the eastern Gulf of Aden: A combined wide-
785 angle, multichannel seismic, and heat flow survey, *Geochem. Geophys. Geosyst.*, *11*(Q07004),
786 doi:10.1029/2009GC002963.

787 Mart, Y., and O. Dauteuil (2000), Analogue experiments of propagation of oblique rifts,
788 *Tectonophysics*, *316*, 121–132.

789 McClay, K. R., and M. J. White (1995), Analogue modelling of orthogonal and oblique rifting, *Mar.*
790 *Pet. Geol.* , *12*(2), 137-151.

791 Menzies, M., and al. (1994), Geology of the Republic of Yemen, in *The Geology and Mineral Resources*
792 *of Yemen*, edited by D. A. McCombe, et al., pp. 21-48.

793 Morrison, J., A. Birse, M. A. Samuel, S. M. Richardson, N. Harbury, and W. F. Bott (1997), The
794 Cretaceous sequence stratigraphy of the Socotran Platform, the Republic of Yemen, *Mar. Pet. Geol.* ,
795 *14*(6), 685-699.

796 Pérez-Gussinyé, M., and T. J. Reston (2001), Rheological evolution during extension at nonvolcanic
797 rifted margins; onset of serpentinization and development of detachments leading to continental
798 breakup, *J. Geophys. Res.*, *106*(3), 3961-3975.

799 Platel, J. P., and J. Roger (1989), Evolution dynamique du Dhofar (Sultanat d'Oman) pendant le
800 Crétacé et le Tertiaire en relation avec l'ouverture du Golfe d'Aden, *Bull. Soc. Geol. Fr.*, *8*(2), 253-263.

801 Ramberg, H. (1981), *Gravity, Deformation and the Earth's Crust*, Academic Press New York.

802 Razin, P., C. Robin, J. Serra Kiel, S. Leroy, N. Bellahsen, and K. Khanbari (2009), Cenozoic evolution of
803 Socotra Island: opening of the Gulf of Aden, in *Fall meeting*, edited, AGU, San Francisco.

804 Ring, U. (2008), Extreme uplift of the Rwenzori Mountains in the East African Rift, Uganda: Structural
805 framework and possible role of glaciations, *Tectonics*, *27*(4), TC4018.

806 Roger, J., J. P. Platel, A. Berthiaux, and J. Le Métour (1992), Geological Map of Hawf with Explanatory
807 Notes; sheet NE 39-16, Ministry of Petroleum and Minerals, Directorate General of Minerals, Oman.

808 Roger, J., J. P. Platel, C. Cavelier, and C. Bourdillon-de-Grisac (1989), Données nouvelles sur la
809 stratigraphie et l'histoire géologique du Dhofar (Sultanat d'Oman), *Bull. Soc. Geol. Fr.*, *2*, 265-277.

Rossi, D., and F. Storti (2003), New artificial granular materials for analogue laboratory experiments: aluminium and siliceous microspheres, *J. Struct. Geol.*, *25*(11), 1893-1899.

Samuel, M. A., N. Harbury, R. Bott, and T. A. M. (1997), Field observations from the Socotran platform: their interpretation and correlation to Southern Oman, *Mar. Pet. Geol.*, *14*(6), 661-673.

Schellart, W. P. (2000), Shear test results for cohesion and friction coefficients for different granular materials: scaling implications for their usage in analogue modelling, *Tectonophysics*, *324*(1-2), 1-16.

Sokoutis, D., G. Corti, M. Bonini, J. Pierre Brun, S. Cloetingh, T. Mauduit, and P. Manetti (2007), Modelling the extension of heterogeneous hot lithosphere, *Tectonophysics*, *444*(1-4), 63-79.

Sonder, L. J. (1990), Effects of density contrasts on the orientation of stresses in the lithosphere: Relation to principal stress directions in the Transverse ranges, California, *Tectonics*, *9*, 761-771.

Tron, V., and J. P. Brun (1991), Experiments on oblique rifting in brittle–ductile systems, *Tectonophysics*, *188*, 71–84.

Upcott, N. M., R. K. Mukasa, C. J. Ebinger, and G. D. Karner (1996), Along-axis segmentation and isostasy in the Western rift, East Africa, *J. Geophys. Res.*, *101*(B2), 3247-3268.

Watchorn, F., G. J. Nichols, and D. W. J. Bosence (1998), Rift-related sedimentation and stratigraphy, southern Yemen (Gulf of Aden). in *Sedimentation and Tectonics in the Rift Basins Red Sea- Gulf of Aden.*, edited by B. Purser and D. Bosence, pp. 165- 189, Chapman & Hall, London.

Wessel, P., and W. H. L. Smith (1995), New version of the Generic Mapping Tools released, *Eos Trans. AGU*, *76*, 329.

Willcox, J. B., and H. M. J. Stagg (1990), Australia's southern margin: a product of oblique extension, *Tectonophysics*, *173*(1-4), 269-281.

Withjack, M. O., and W. R. Jamison (1986), Deformation produced by oblique rifting, *Tectonophysics*, *126*(2-4), 99-124.

Zoback, M. L. (1992), First- and Second-Order Patterns of Stress in the Lithosphere: The World Stress Map Project, *J. Geophys. Res.*, *97*(B8), 11703-11728.

Figure captions

Table 1: Main physical properties of natural and analogue materials used in our models.

Figure 1: Deforming box used for the models (56 X 30 X 30 to 50 cm3). A drawer without bottom is pulled by a screw jack, which represent the direction of extension. The drawer arms are of different lengths, so that they create two lateral velocity discontinuities imposing an oblique direction of deformation.

Figure 2: Strength profiles for the experimental lithosphere and for the heterogeneity. The cohesion is decreasing for low depth (low vertical stress). The intersection of the brittle failure straight line with the differential stress axe corresponds to the fracture strength under uniaxial compression with zero confining pressure [*Schellart*, 2000].

Figure 3: Top views of the model A during extension (amount of extension throughout the entire model). Bottom side lighting direction. Line-drawings are available for the first stages of the model with the azimuthal distribution of the percentage of total length for each segment population. Blue: rift-parallel segments. Green: intermediate segments. Red: displacement-normal segments. Circled numbers correspond to the stages described in the text. Important clockwise block rotations (orange arrows) are observed during the evolution of this model leading to the formation of triangular grabens (blue) and highly deformed area (green).

Figure 4: Top views of the model B during extension (amount of extension throughout the entire model). Bottom side lighting direction. Line-drawings are available for the first stages of the model with the azimuthal distribution of the percentage of total length for each segment population. Blue: rift-parallel segments. Green: intermediate segments. Red: displacement-normal segments. Circled numbers correspond to the stages described in the text.

Figure 5: Time-evolution of the fault population during the first stages of development of the models A (uniform lithosphere) and B (with a lithospheric heterogeneity) with increasing extension. Blue: rift-parallel segments. Green: intermediate segments. Red: displacement-normal segments. A-D: number of segments evolution. B-E: total cumulated length percentage. C-F: total cumulated length. Circled numbers correspond to the stages described in the text.

Figure 6: Top views of the center of the model A during extension. Bottom side lighting direction. Circled numbers correspond to the stages described in the text.

Figure 7: Top views of the center of the model B during extension. Bottom side lighting direction. Circled numbers correspond to the stages described in the text.

Figure 8: Differential vertical movements obtained by the subtraction of two successive DEM (2 minutes spaced) for the model A and for increasing extension amount. Active faults are thus highlighted for a specific time interval. Circled numbers correspond to the stages described in the text.

Figure 9: Differential vertical movements obtained by the subtraction of two successive DEM (2 minutes spaced) for the model B and for increasing extension amount. Active faults are thus highlighted for a specific time interval. Circled numbers correspond to the stages described in the text.

Figure 10: Evolution of the topography (from DEM) for model A and B along two profiles: extension-parallel and rift-perpendicular cross-sections. See profiles localization on the topographic maps.

Figure 11: Model extension-parallel cross-sections (see location on Figure 10, 0° lines, no vertical exaggeration) and comparison with the orthogonal model of *Brun and Beslier* [1996]. Analogue materials, layer thicknesses and extension velocities are comparable. The amount of extension is indicated in percents. Cross-sections of models A and B are reconstructed from interfaces geometry (see section 2.4.3), whereas cross-section of the orthogonal model was observed on frozen dissected model. Boudinage of the brittle mantle, which localizes deformation at depth and shear zones in the ductile layers lead to the uplift and final exhumation of the mantle in orthogonal extension. Because of the less localized deformation in oblique extension (wider rifted zone) and of the lack of syn-rift sedimentation, larger extension will be needed, and particularly in model A.

Figure 12: Photographs of the top of the brittle mantle for models A and B, taken after the removal of the brittle and ductile crust layers. Note the exhumation of the reddish ductile mantle in the center of the rift in model B. Bottom side lighting direction.

Figure 13: Line drawing of the models A and B after 20% extension. Major faults are reported with their dip.

Figure 14: Line-drawing of the three main steps in the evolution of model A. See text for explanation. Drawings are rotated in order to fit the opening direction of the Gulf of Aden (N020°E, white arrows). Black arrows represent the local stresses induced by thickness variation.

Figure 15: Fault distribution (percentage of total length vs. fault azimuth) for different analogue models of oblique rifting and comparison to the Gulf of Aden (measured faults onland).

Figure 16: Structural reconstruction of the conjugate margins of the oriental Gulf of Aden at the end of the Ocean-Continent Transition formation [after *d'Acremont et al.*, 2006]. Synthesis from field work and seismic reflection data [*Beydoun and Bichan*, 1969; *Platel and Roger*, 1989; *Roger et al.*, 1989; *Roger et al.*, 1992;

915 ***Menzies and al.*, 1994; *Fantozzi*, 1996; *Birse et al.*, 1997; *Brannan et al.*, 1997; *Morrison et al.*, 1997; *Samuel***
916 ***et al.*, 1997; *Watchorn et al.*, 1998; *Khanbari*, 2000; *Lepvrier et al.*, 2002; *Leroy et al.*, 2004; *d'Acremont et al.*,**
917 **2005; *Bellahsen et al.*, 2006; *Razin et al.*, 2009; *Autin et al.*, 2010; *Leroy et al.*, 2010].**

918

919

Tables

			Nature	Model
Crust	Upper crust	Thickness	20 km	1.5 cm
		Density	2.6 - 2.8 $g.cm^{-3}$	1.2 $g.cm^{-3}$
	Lower crust	Thickness	10 km	0.7 cm
		Density	2.9 $g.cm^{-3}$	1.25 $g.cm^{-3}$
		Viscosity	10^{21} Pa.s	4.10^{4} Pa.s
Mantle	Lithospheric brittle mantle	Thickness	~ 12 km	0.8 cm
		Density	3.3 $g.cm^{-3}$	1.2 $g.cm^{-3}$
	Lithospheric ductile mantle	Thickness	~ 50 km	2 cm
		Density	3.3 $g.cm^{-3}$	1.33 $g.cm^{-3}$
		Viscosity	10^{23} Pa.s	7.10^{4} Pa.s
	Asthenosphere	Density	3.2 - 3.4 $g.cm^{-3}$	1.41 $g.cm^{-3}$
		Viscosity	10^{19} Pa.s	10 Pa.s

Table 1

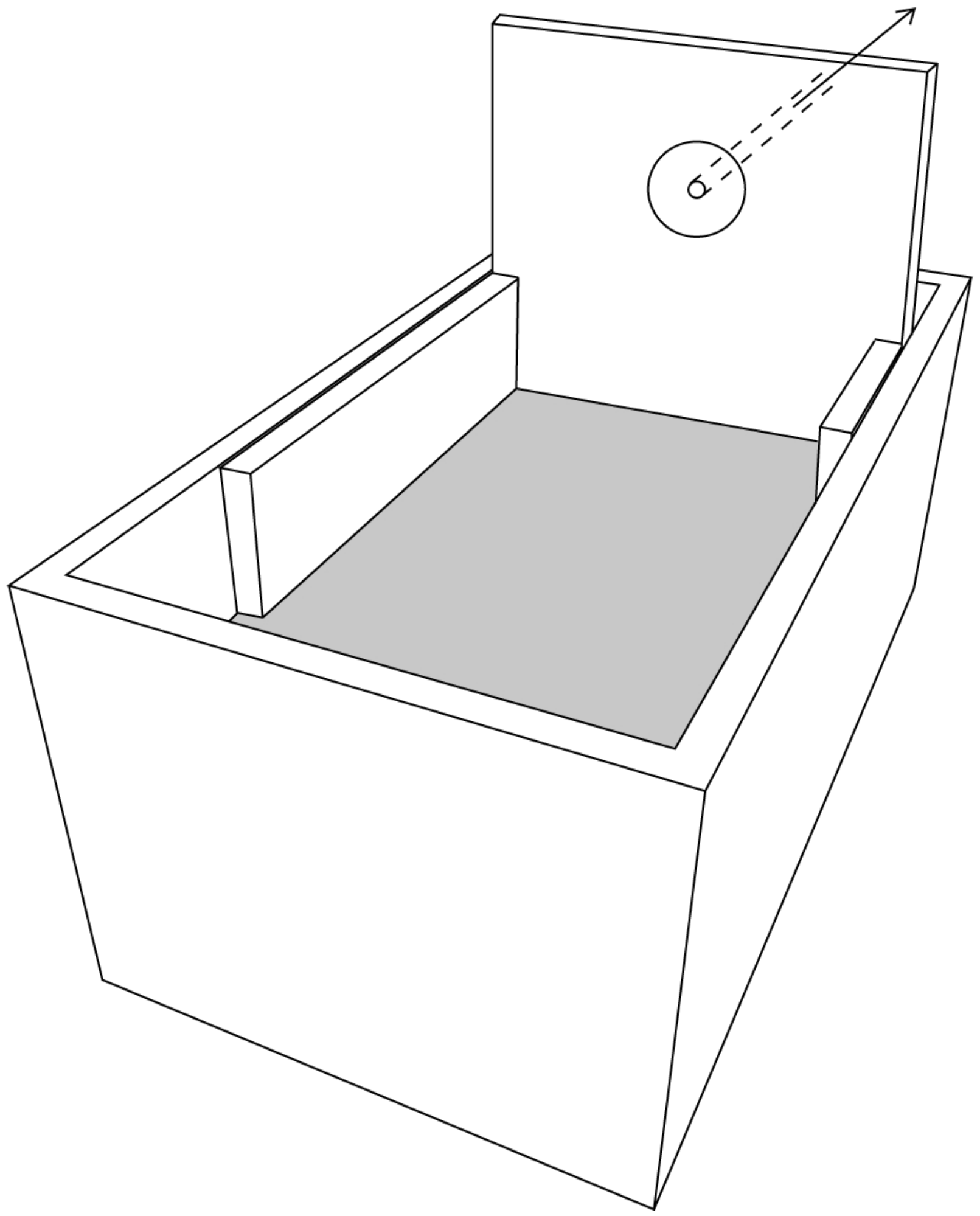
α

Models rheology

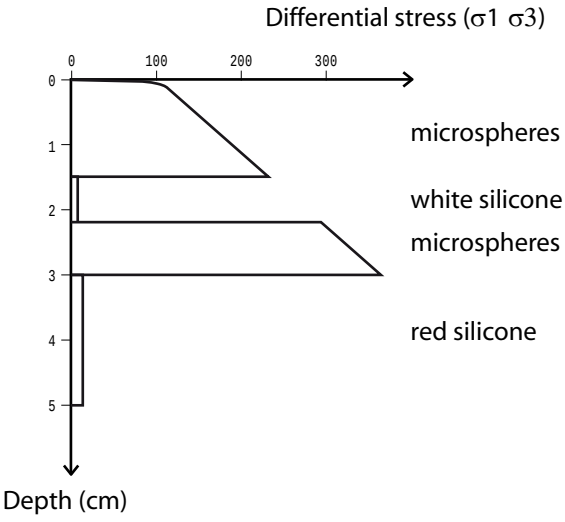

Heterogeneity rheology

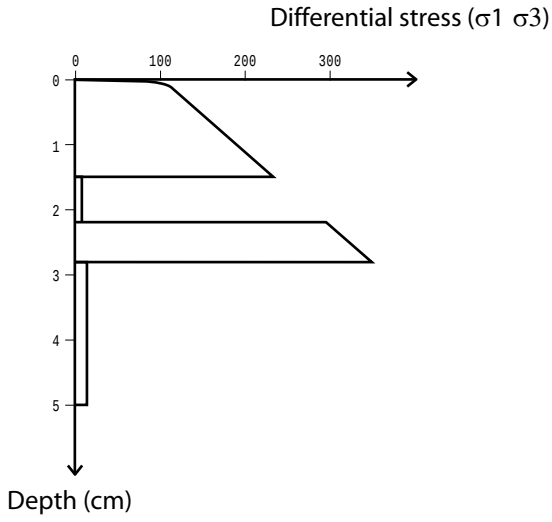

① 2.5%

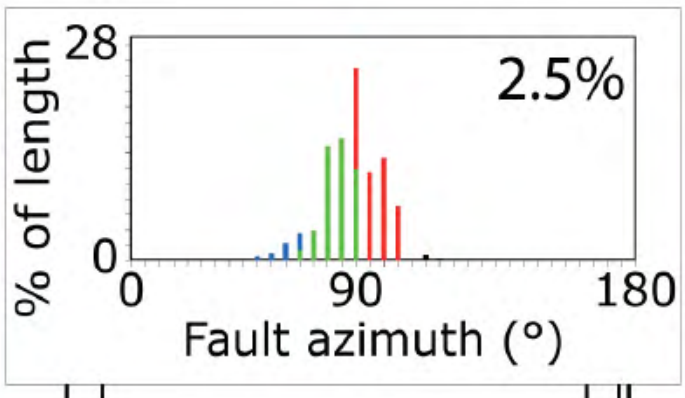

② 4%

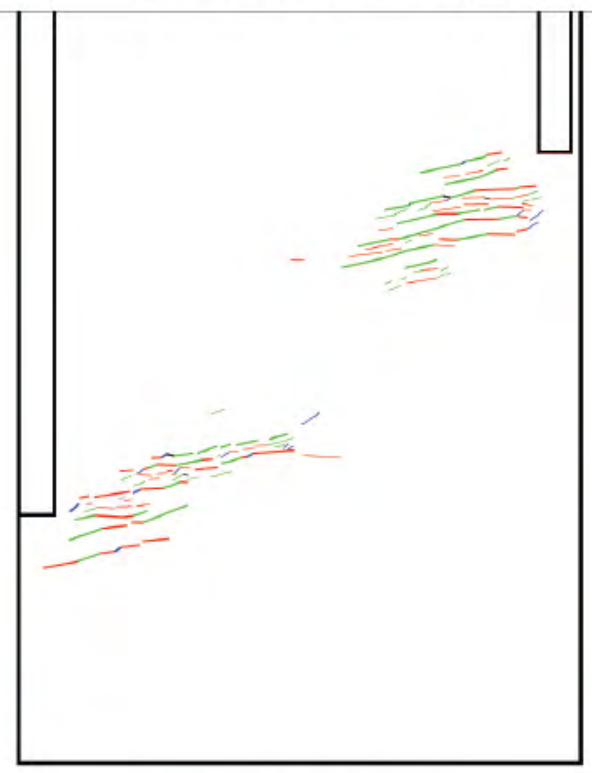

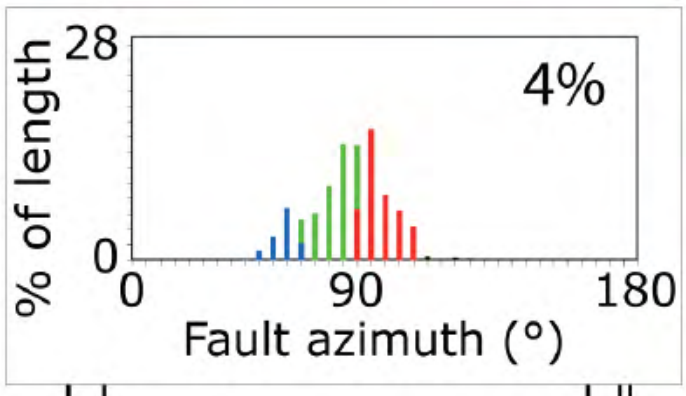

② 6.5%

② 10%

③ 16%

③ 21%

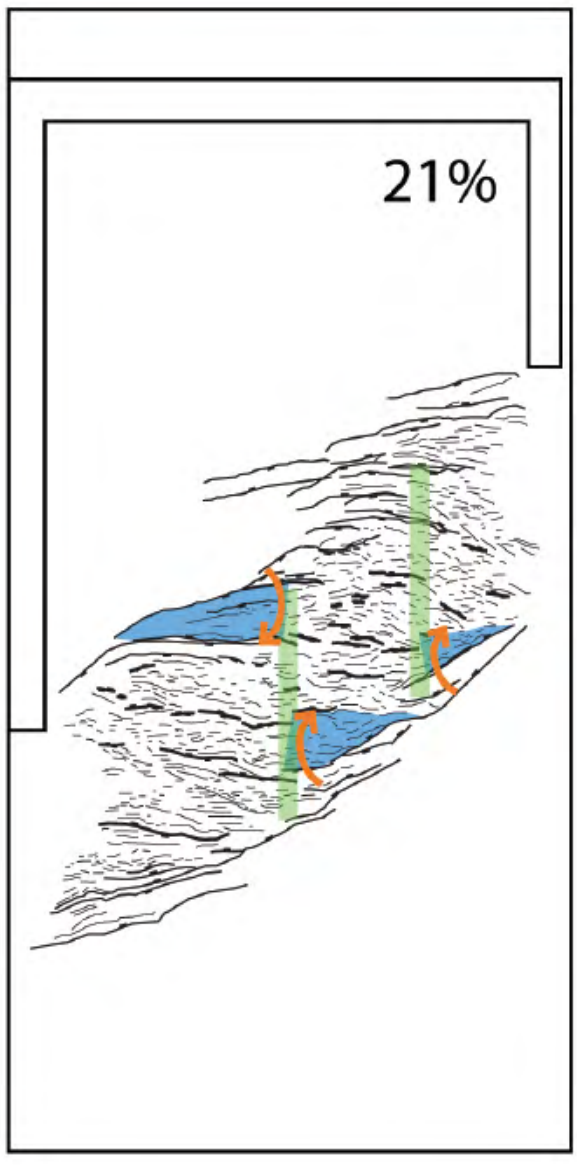

FIGURE 3

① 2.5%

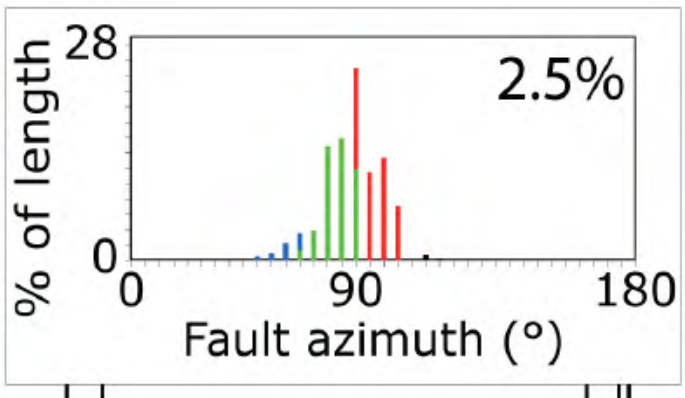

② 4%

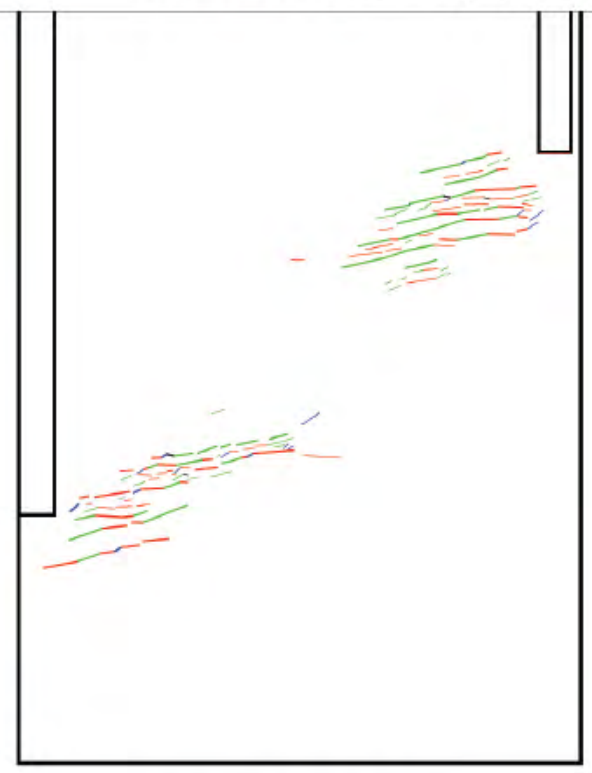

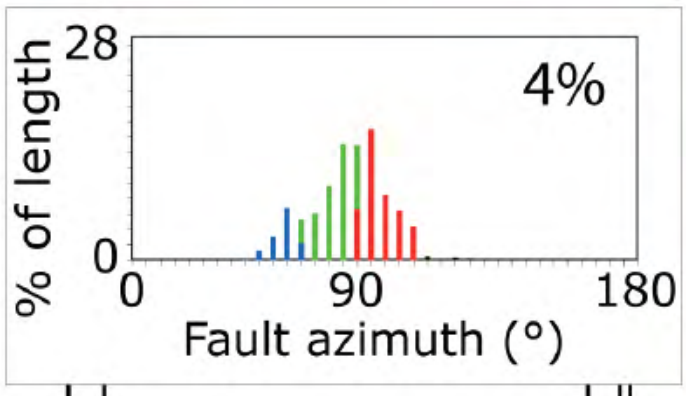

② 6.5%

② 10%

③ 16%

③ 21%

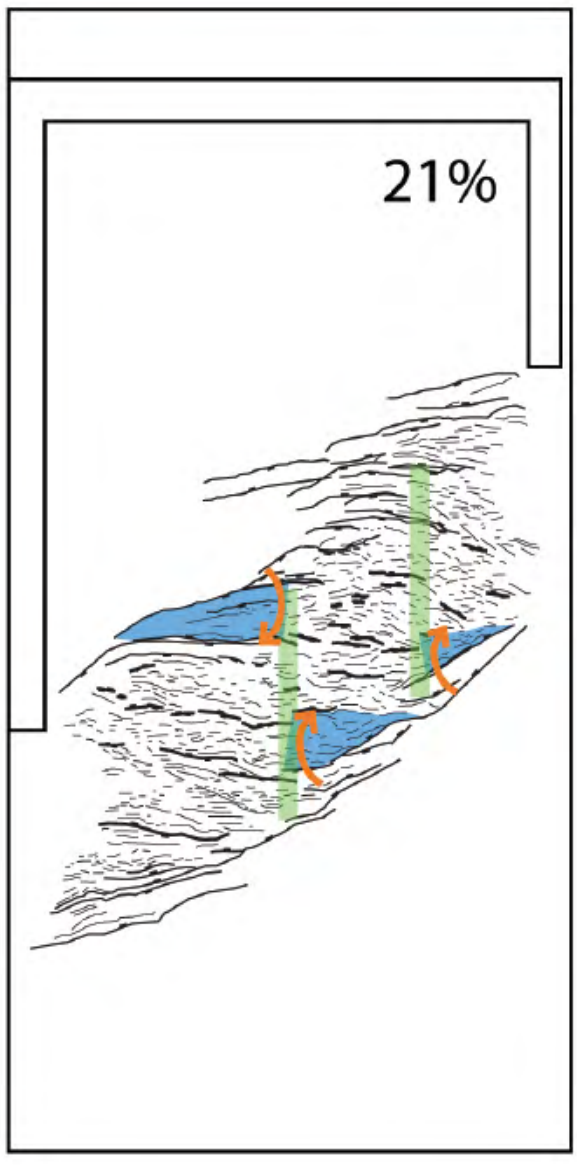

FIGURE 3

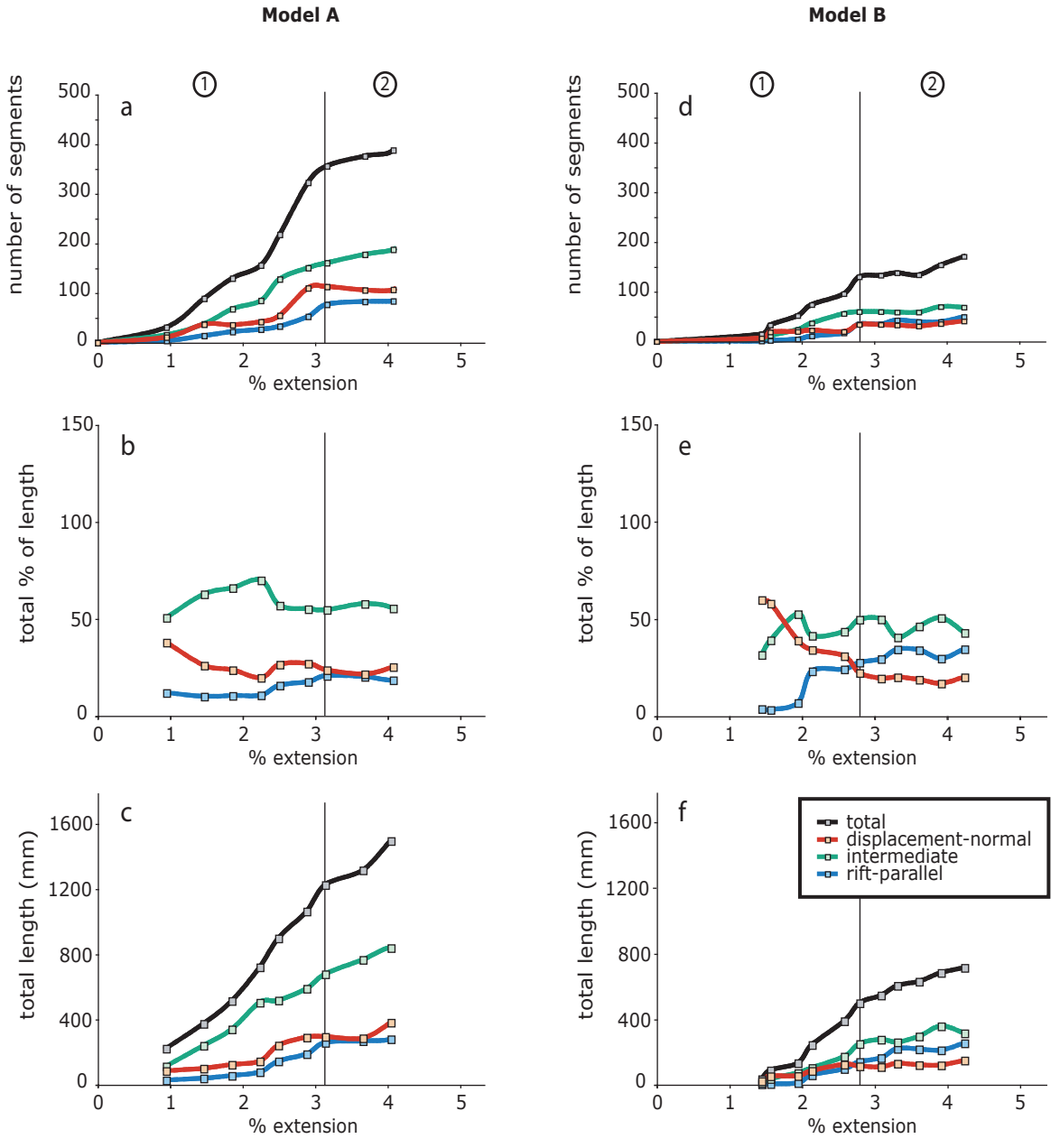
Model A
Model B
a
b
c
d
e
f
①
②
number of segments
total % of length
total length (mm)
% extension
total
displacement-normal
intermediate
rift-parallel

① 3%

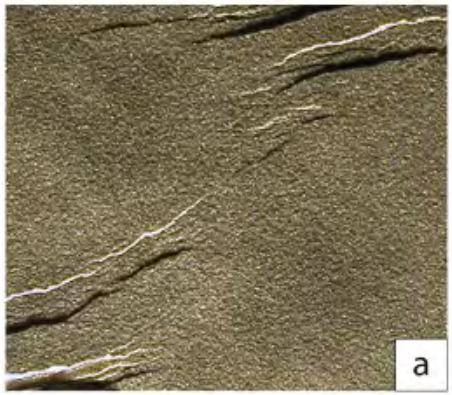

② 4%

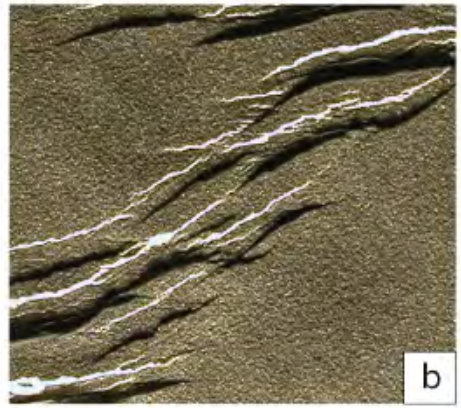

② 6.5%

5 cm

② 10%

③ 16%

③ 21%

FIGURE 6

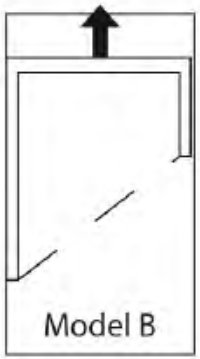

② 3%

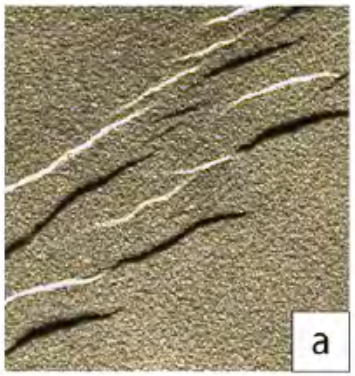

② 4%

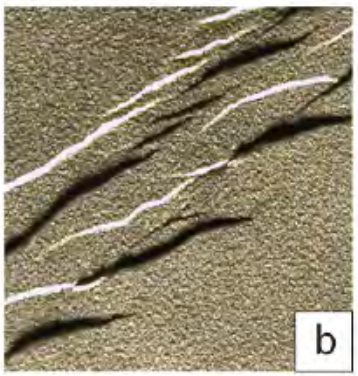

② 7%

5 cm

② 10.5%

③ 16.5%

③ 19.5%

FIGURE 7

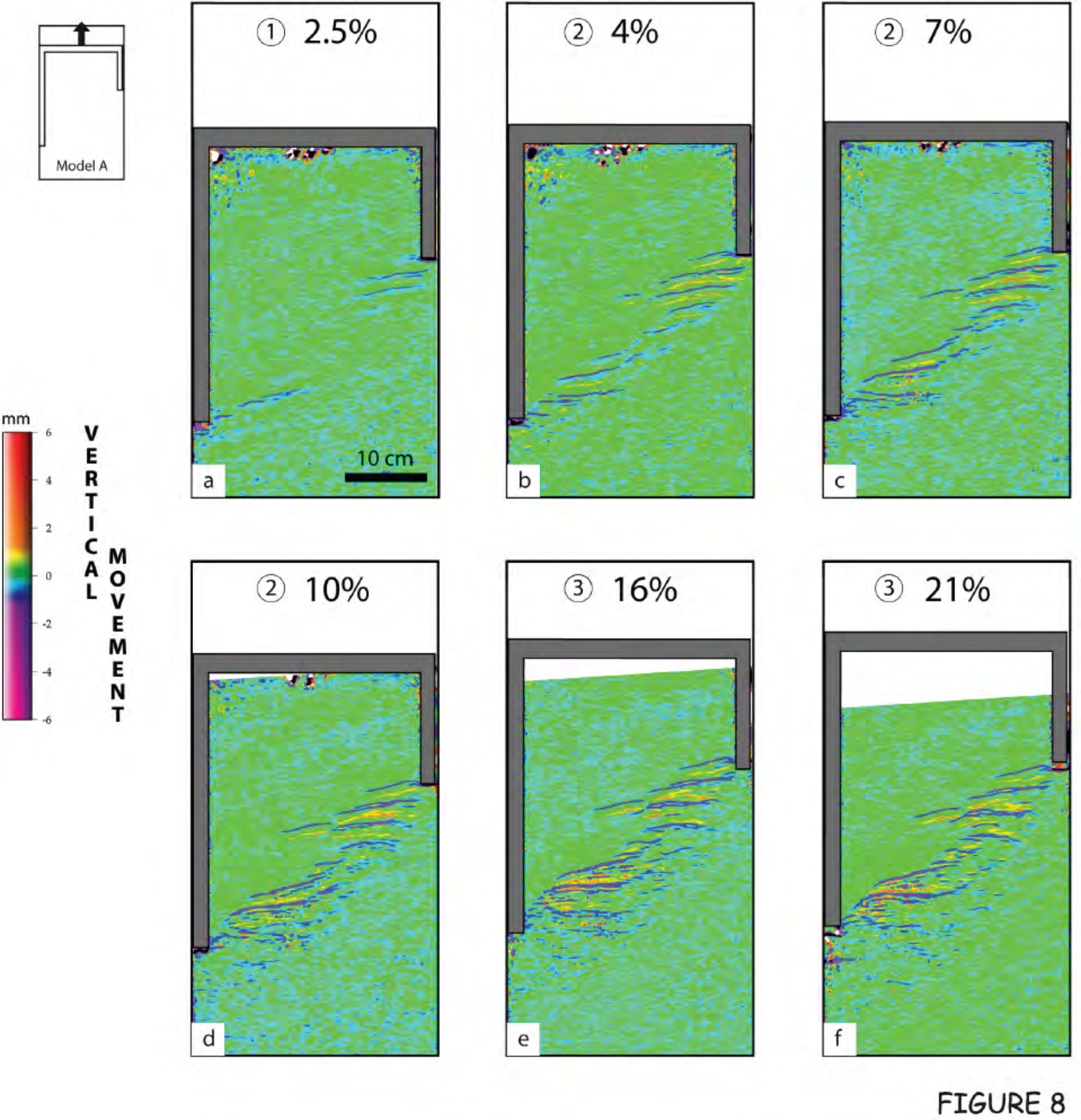
Model A
① 2.5%
② 4%
② 7%
10 cm
a
b
c
mm
6
4
2
0
-2
-4
-6
VERTICAL MOVEMENT
② 10%
③ 16%
③ 21%
d
e
f

FIGURE 8

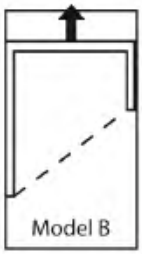
Model B

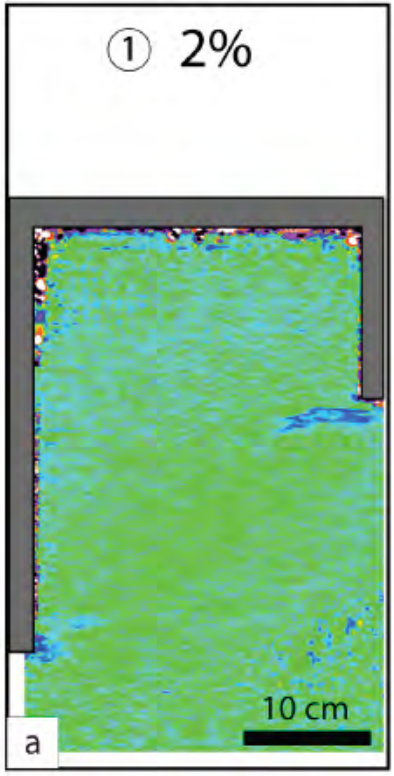
① 2%
10 cm
a

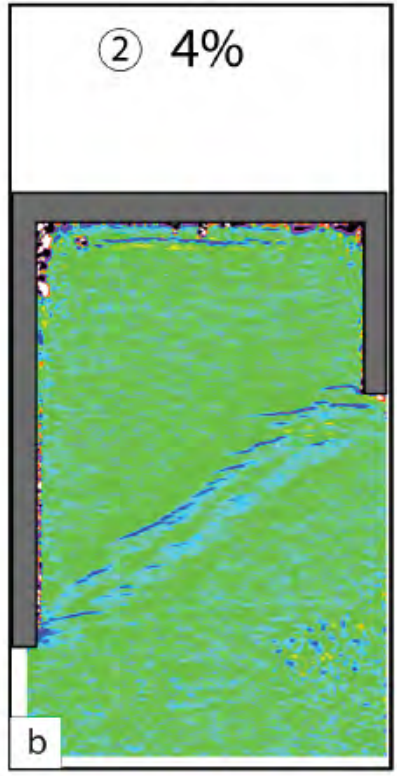
② 4%
b

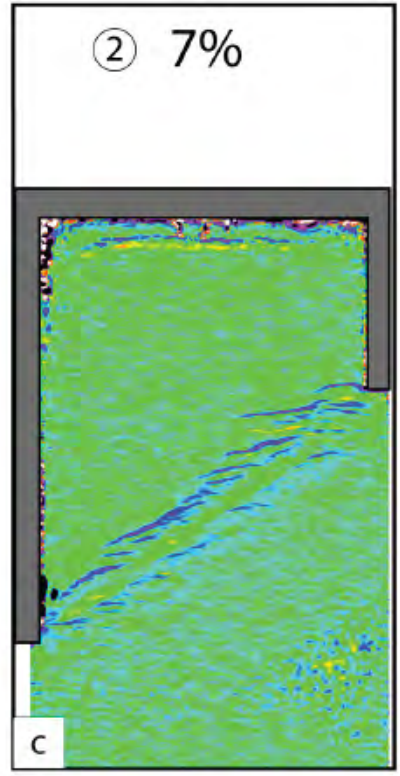
② 7%
c

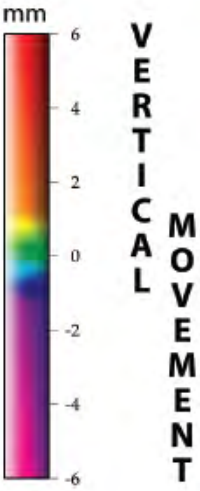
mm
6
4
2
0
-2
-4
-6
VERTICAL MOVEMENT

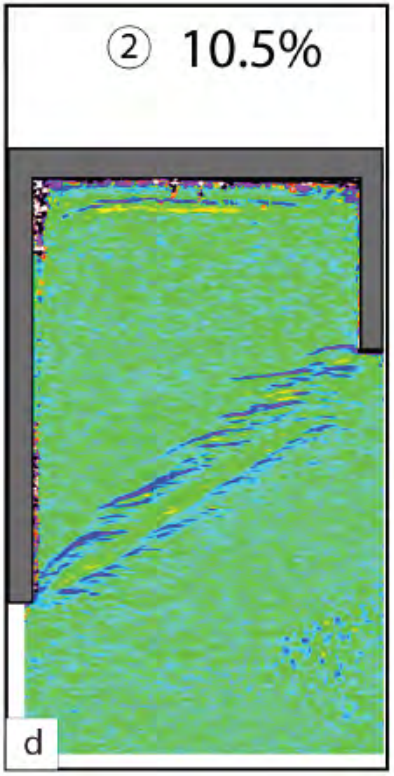
② 10.5%
d

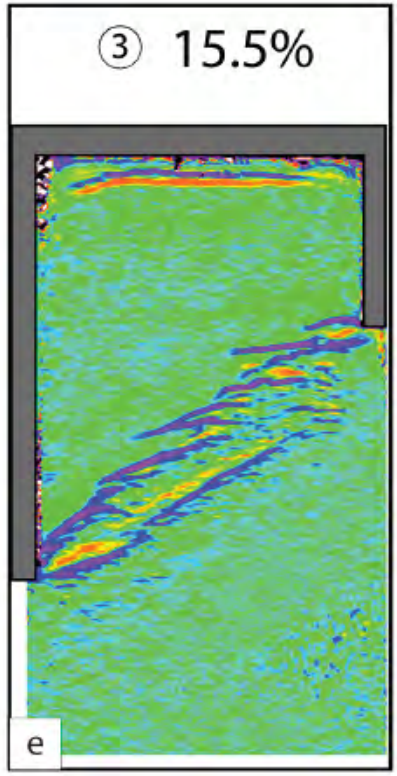
③ 15.5%
e

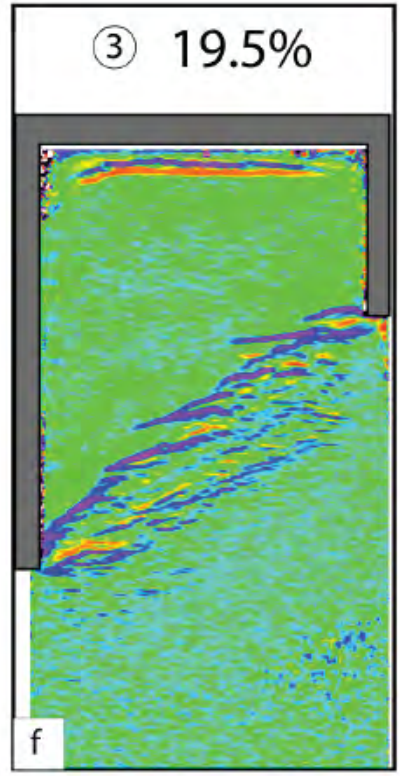
③ 19.5%
f

FIGURE 9

Model A

Model B

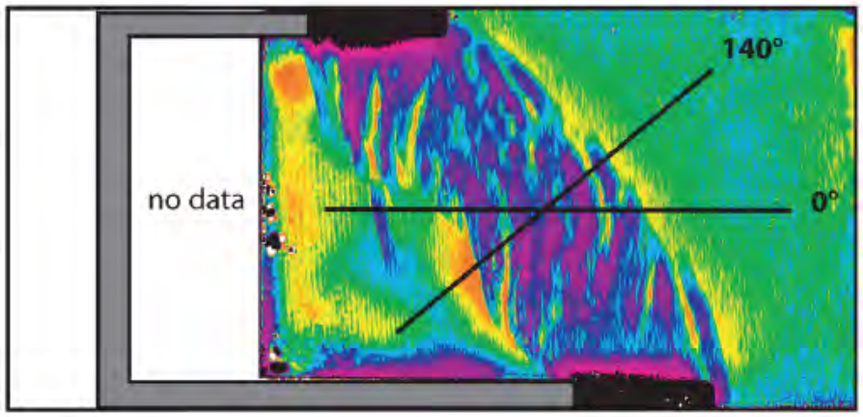

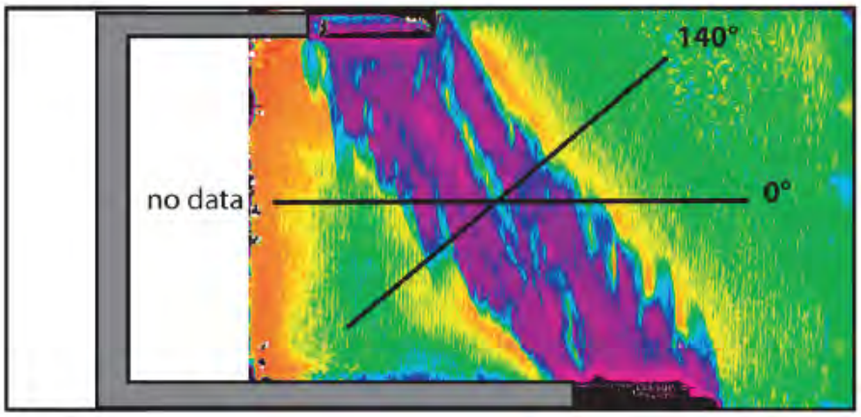

extension rate (%)

rift-perpendicular cross-section (140°)

21
19
17.5
16
14
12
10.5
9
7
5.5
4
2

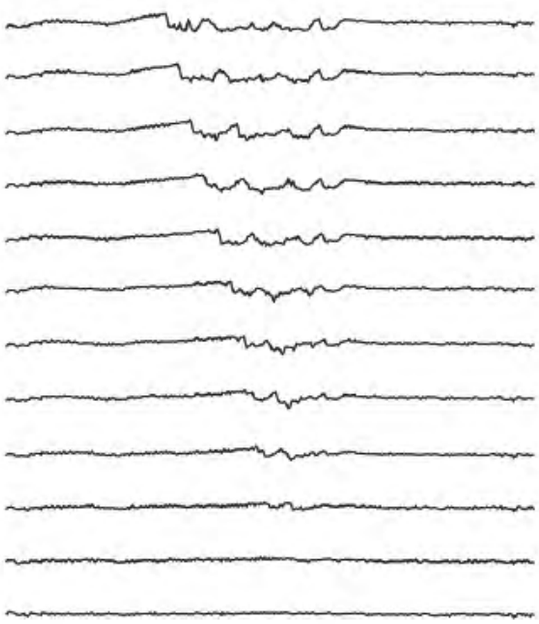

extension rate (%)

rift-perpendicular cross-section (140°)

19.5
16.5
15.5
13.5
11.5
10
8.5
6.5
5
3.5
2

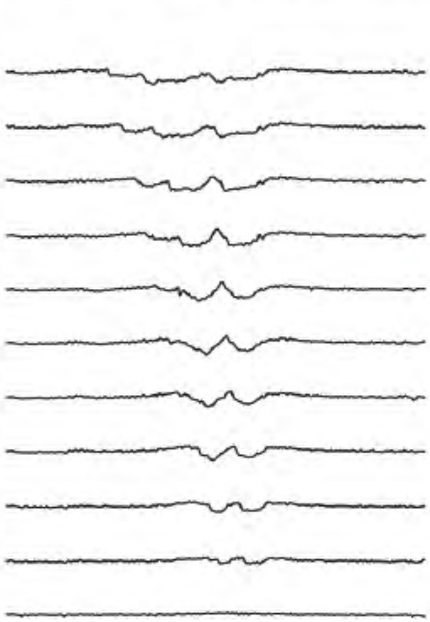

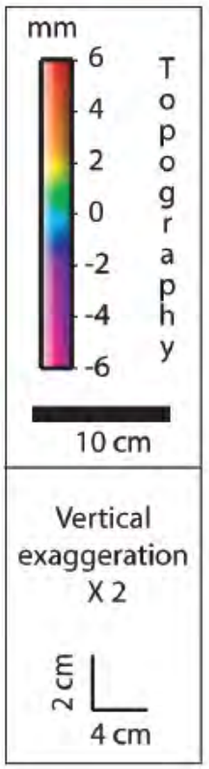

extension-parallel cross-section (0°)

21
19
17.5
16
14
12
10.5
9
7
5.5
4
2

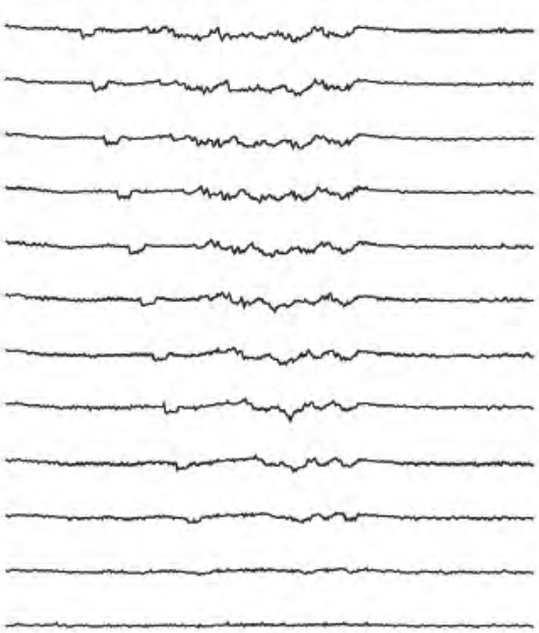

extension-parallel cross-section (0°)

19.5
16.5
15.5
13.5
11.5
10
8.5
6.5
5
3.5
2

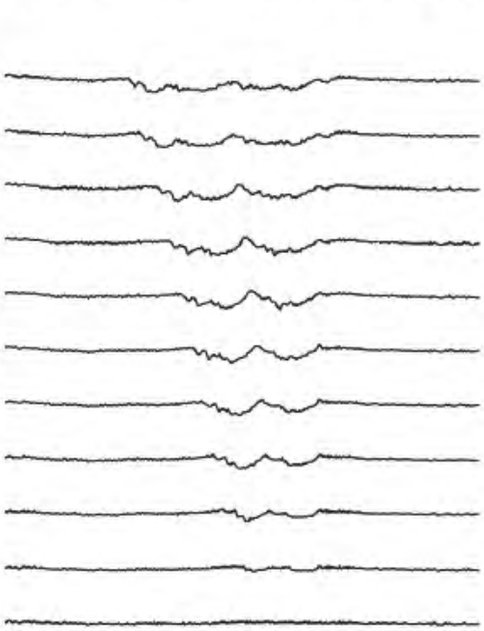

Model A : extension-parallel cross-sections 21%

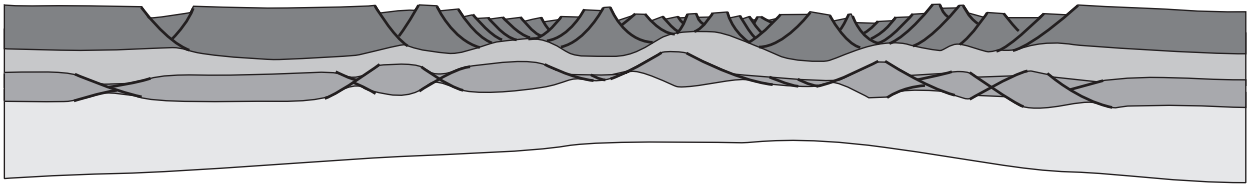

Model B : extension-parallel cross-sections 19.5%

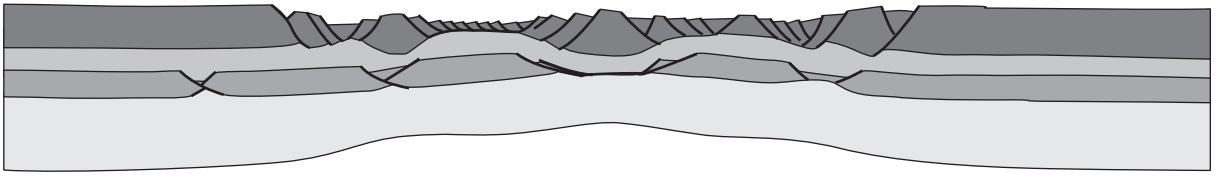

Orthogonal model (Brun and Beslier, 1996) 9%

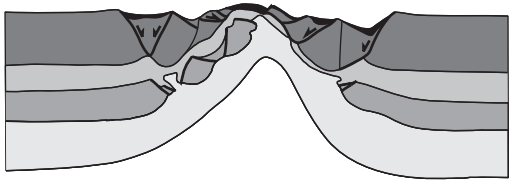

5 cm

no vertical exaggeration

Syn-rift sediments

Brittle crust

Ductile crust

Brittle upper mantle

Ductile upper mantle

MODEL A

MODEL B

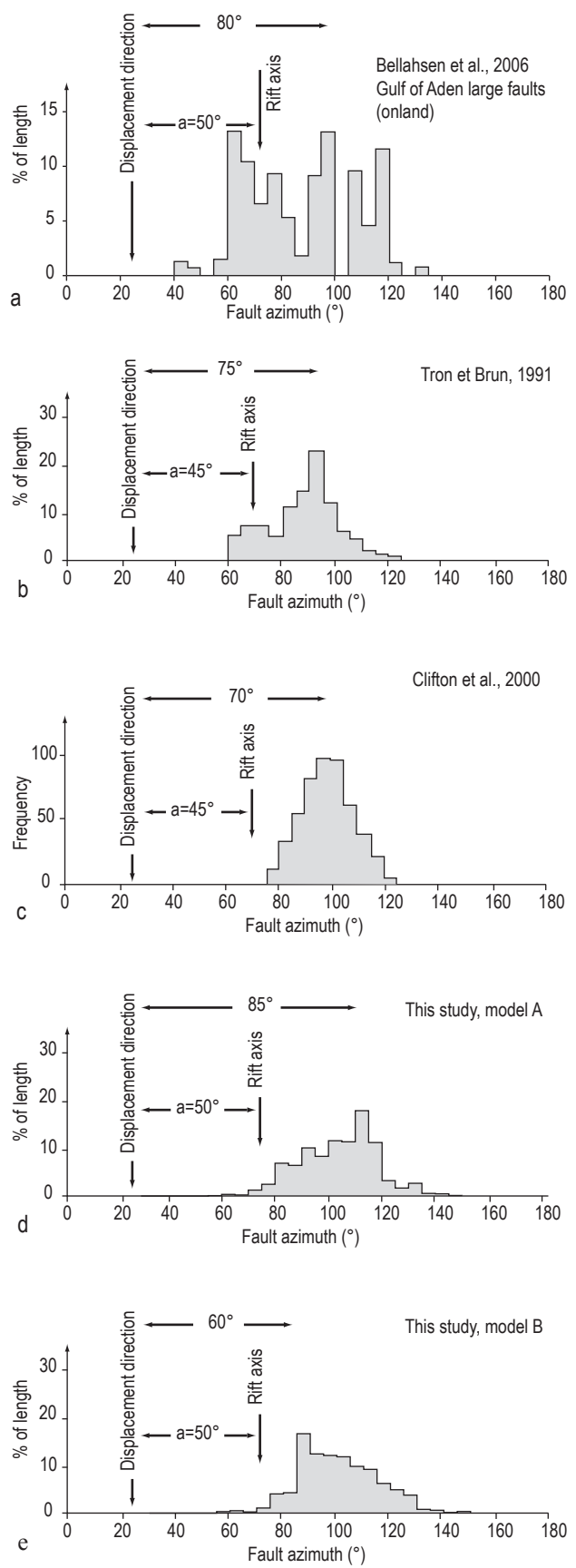
80°
Displacement direction
Rift axis
Bellahsen et al., 2006
Gulf of Aden large faults
(onland)
a=50°
% of length
15
10
5
0
0 20 40 60 80 100 120 140 160 180
Fault azimuth (°)
a
75°
Tron et Brun, 1991
Displacement direction
Rift axis
a=45°
% of length
30
20
10
0
0 20 40 60 80 100 120 140 160 180
Fault azimuth (°)
b
Clifton et al., 2000
70°
Displacement direction
Rift axis
a=45°
Frequency
100
50
0
0 20 40 60 80 100 120 140 160 180
Fault azimuth (°)
c
85°
This study, model A
Displacement direction
Rift axis
a=50°
% of length
30
20
10
0
0 20 40 60 80 100 120 140 160 180
Fault azimuth (°)
d
60°
This study, model B
Displacement direction
Rift axis
a=50°
% of length
30
20
10
0
0 20 40 60 80 100 120 140 160 180
Fault azimuth (°)
e

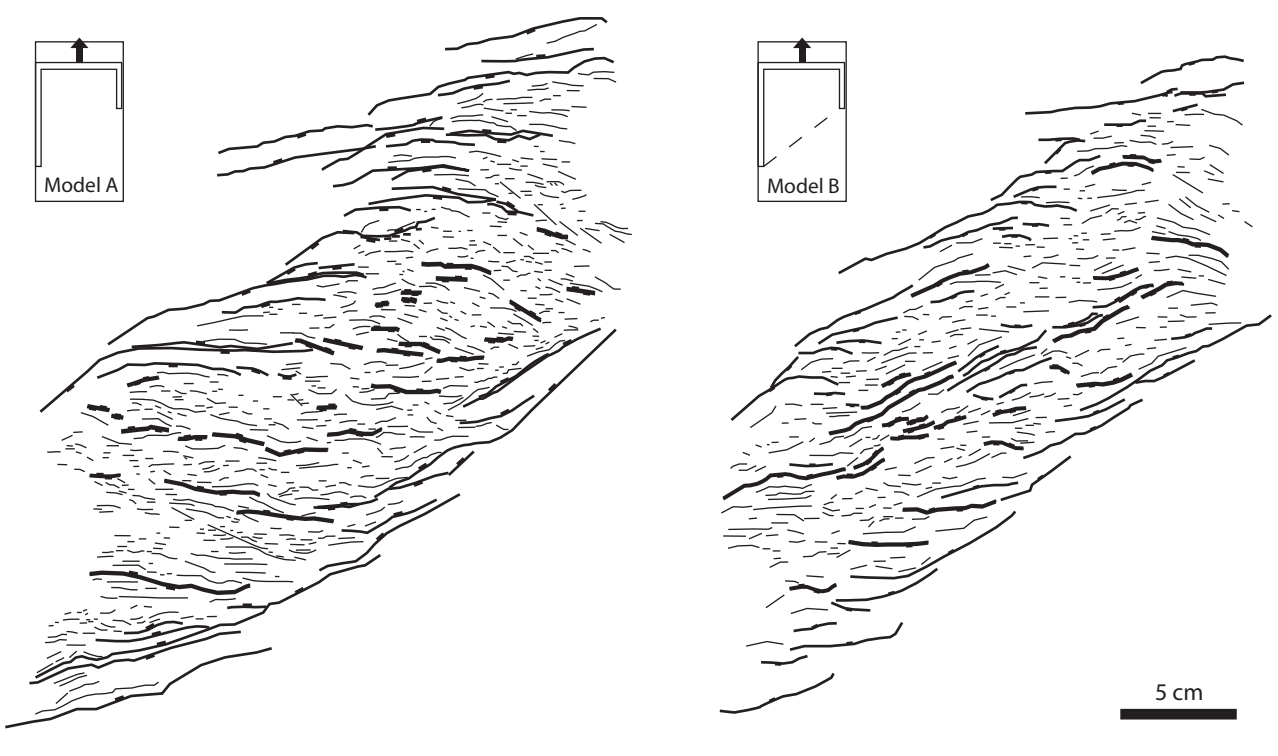
Model A
Model B
5 cm

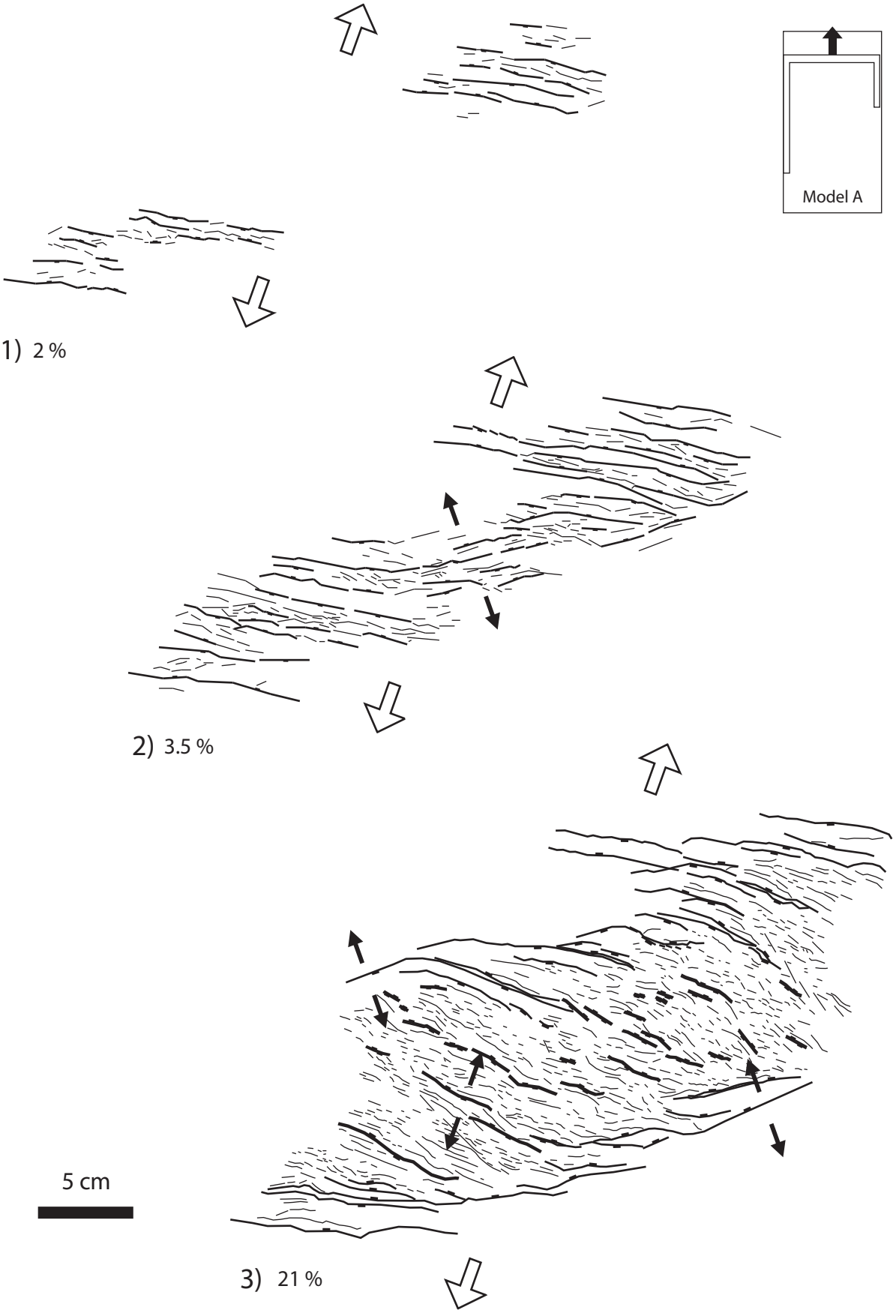
Model A
1) 2 %
2) 3.5 %
3) 21 %
5 cm

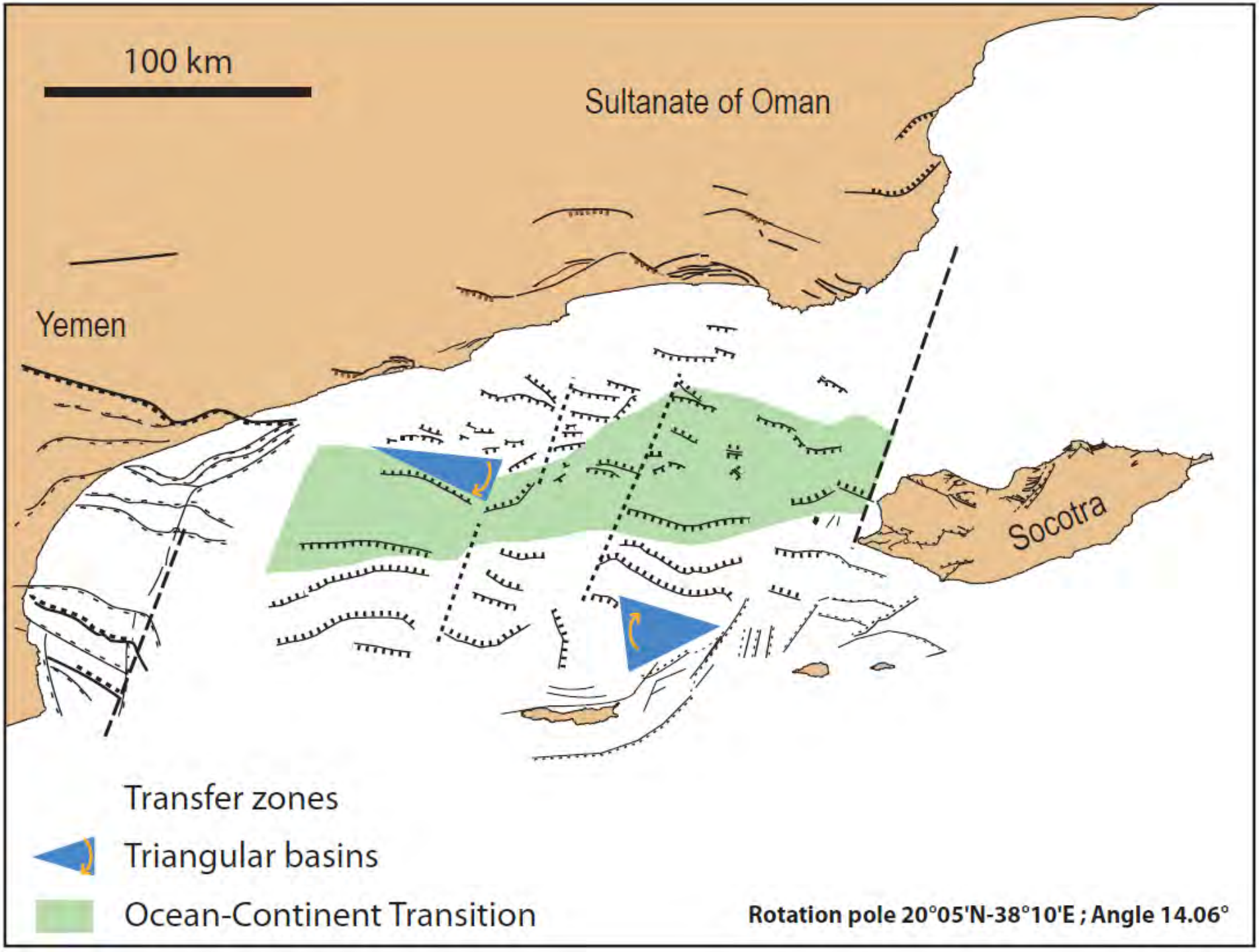
100 km
Sultanate of Oman
Yemen
Socotra
Transfer zones
Triangular basins
Ocean-Continent Transition
Rotation pole 20°05'N-38°10'E ; Angle 14.06°